Searches for New Physics in final states containing leptons, b-jets and $E_{\mathrm{T}}^{\mathrm{miss}}$ at the ATLAS detector

UNIVERSITY OF LIVERPOOL

Thesis submitted in accordance with the requirements of the University of Liverpool for the degree of Doctor in Philosophy by

Matthew James Sullivan

Department of Physics
Oliver Lodge Laboratory
University of Liverpool

September 2020

Abstract

This is my abstract.

Declaration

I hereby confirm this work is my own, except where other works are referenced. This work has not previously been submitted to any institute, including this one. This thesis does not exceed the relevant word count.

Matthew James Sullivan

Acknowledgements

During my eight years at the University of Liverpool, the people helping to make it such a memorable period of my life have become innumerable, and to thank each and every person would require an equally long period of time. For those not acknowledged by name I can only give my thanks for being involved in this part of my life. It has been a true privilege to call this city my home and be a part of the Department of Physics throughout.

The first of many thanks goes to my mum, my dad and my sister, for their endless and unwavering support throughout my PhD. The level of support you all offer continues to astound me and I can only offer my gratitude in return. An honourable mention must go to my niece, Charlotte, who was born halfway through my PhD and has been the best niece one could ask for, although these words are, for now, lost on you.

Secondly, many thanks are owed to the non-physics friends, who have given me respite from the challenges of my PhD. Particularly, Holly, Brad, Pete, Alex, Ellie and Sean, who have supported and encouraged me through challenging professional and personal times. Your continued reminder to write this Thesis, however, is unforgiveable. Additionally, a big thanks to Hannah, who for the last ten years has been putting up with my nonsense, and hopefully will continue to do so. I hope over time I can begin to pay back the levels of support you have all given me.

These acknowledgements would be incomplete without a mention to the circumstances within which a large portion of it was written. The COVID-19 pandemic has had a devastating impact on individuals and families the world-over, causing both physical and mental struggle. On a personal level, numerous thanks are owed for enabling me to submit this work in this turbulent time. Firstly, to UKRI, for their generous financial support, enabling me to continue my work during these challenging times. Secondly, thanks are owed to the NHS, both due to their handling of the national crisis and for their continued healthcare support during, undoubtedly, the most stressful period of my life. However, the period of national lockdown due to the coronavirus has also provided unforeseen opportunities for personal development, and I submit this work having gained far more than anticipated. Countless thanks are owed to Jess, for managing to keep my stress-levels under control, for

the walks, the talks and the laughs. Without you, this work would have been submitted in a much heavier fashion.

Of course, many thanks are owed to the physics community within which I have been immersed. Firstly, to the Liverpool ATLAS group, who welcomed me into the collaboration in 2016 and have supported me throughout my PhD. The group, and the department, provided me with some incredible opportunities, for which I am extremely grateful. Secondly, to all of the physics friends, who have listened to my rants, help spot the bugs I couldn't find, and bluntly point out when I'm being stupid. Special thanks must go to James, Chips and Lauren for dealing with me when at my most difficult, and for the frequent trips to the pub, both in Liverpool and Geneva.

Finally, to my excellent supervisors, Monica D'Onofrio and Yanyan Gao. You have pushed me to levels beyond what I imagined I could achieve and have given me amazing opportunities for professional development. I can only apologise for being slow and stupid, and am extremely grateful for your patience in supervision.

Contents

List of Figures

List of Tables

Part I

Searches for New Physics in Run-2 ATLAS data

Chapter 1

Searches for $\tilde{\chi}_1^{\pm}\tilde{\chi}_2^0$ pair-production

This Chapter presents an overview of searches for the pair-production of a chargino, $\tilde{\chi}_1^{\pm}$ and next-to-lightest neutralino, $\tilde{\chi}_2^0$, performed during the Run-2 period of data-taking. This Chapter focuses mainly on an analysis performed using data taken in 2015-2016, totalling 36.1fb^{-1}. Later in this Chapter, the results of an analysis using the full Run-2 dataset of 139fb^{-1} is presented, along with additional studies using machine learning to improve the sensitivity to the signal. Chapter 4 presents sensitivity studies for this signal at the High-Luminosity LHC, using a dataset of 3000fb^{-1} collected at $\sqrt{s} = 14$ TeV.

A search for $\tilde{\chi}_1^{\pm}\tilde{\chi}_2^0$ pair-production decaying via the Wh signature was undertaken in Run 1 using 20.3fb^{-1} taken at $\sqrt{s} = 8$ TeV [1], targeting leptonic W boson decays, and $h \to b\bar{b}$, $h \to \gamma\gamma$, $h \to WW^*/ZZ^*/\tau\tau$ decays. 95% confidence limits were set on this signal, excluding the process upto $\tilde{\chi}_1^{\pm}/\tilde{\chi}_2^0$ masses of around 275 GeV for a massless $\tilde{\chi}_1^0$. The exclusion limit for the individual channels, as well as the statistical combination of all channels, is shown in Figure 1.1.

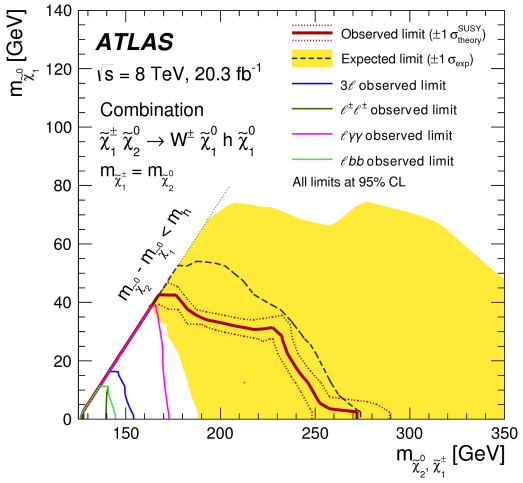

Figure 1.1: A plot showing the four exclusion limits obtained from searches for $\tilde{\chi}_1^{\pm}$ $\tilde{\chi}_2^0$ pair-production with the Wh signature during the Run-1 data-taking period.

The Run-1 analysis had limited sensitivity to the signal model, as shown in Figure 1.1, where the yellow band around the combined limit shows the size of the statistical and systematic uncertainty on the SM background.

1.1 SUSY signal model

The results of the analysis presented in this Chapter and in Chapter 4 are interpreted in the context of a simplified SUSY model [2, 3], in which the $\tilde{\chi}_1^{\pm}$ and $\tilde{\chi}_2^0$ are unstable and each decay to the lightest neutralino, $\tilde{\chi}_1^0$, via a SM W boson and Higgs boson. The decay channel targeted in this Chapter and in Chapter 4 require the W boson to decay leptonically, $W \to \ell\nu$, while the Higgs boson decays to two b-tagged jets, $h \to b\bar{b}$. The Higgs boson in this process, h, is the lightest CP-even Higgs from the extended SUSY Higgs sector and is assumed to be a SM-like Higgs boson, with $m_{\mathrm{h}} = 125$ GeV and with the branching fraction of $\mathrm{BR}(h \to b\bar{b}) = 58\%$. Complimentary decay channels targeting the all-hadronic, $Wh \to qq'b\bar{b}$, and the single lepton plus photons, $Wh \to \ell\nu\gamma\gamma$, decays allow the reconstruction of the Higgs boson, while the same-sign two-lepton and the three-lepton channels are sensitive to the $h \to WW^*/ZZ^*/\tau\tau$ decays. Dedicated searches also target the decay of the $\tilde{\chi}_2^0$ to the Z boson [4,5], targeting the decay of the Z boson to two charged leptons. A diagram of the signal process relevant for this Chapter is shown in Figure 1.2.

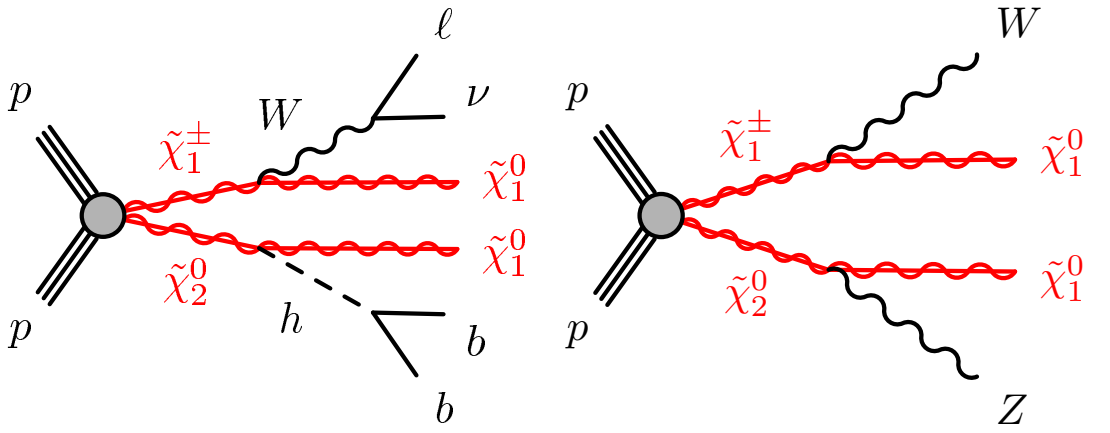

Figure 1.2: Diagram showing $\tilde{\chi}_1^{\pm}\tilde{\chi}_2^0$ pair-production, with the chargino and neutralino decaying via a SM W boson and a Higgs (1.2a), and a Z boson (1.2b), respectively.

SUSY models have an enormous parameter space with over 100 free parameters, such as the sparticle masses and couplings. Simplified models vastly reduce the number of free parameters, such that a single analysis can be sensitive to a large region of the SUSY model phase space. In this analysis, it is assumed that the branching ratios of the $\tilde{\chi}_1^{\pm} \to W\tilde{\chi}_1^0$ and $\tilde{\chi}_2^0 \to h\tilde{\chi}_1^0$ are both 100%, while the mass of the Higgs boson, m_h, is assumed to be

SM-like. The only free parameters of the simplified model used in both this Chapter and Chapter 4 are m($\tilde{\chi}_1^{\pm}$), m($\tilde{\chi}_2^0$) and m($\tilde{\chi}_1^0$).

1.2 Event selection

Candidate events for this analyses are first selected using a set of loose, preliminary selections, known as 'preselection'. The preselection cuts, summarised in Table 1.1, target events with an event topology of a single lepton, two b-jets and $E_{\mathrm{T}}^{\mathrm{miss}}$. All events are required to have exactly 1 electron or muon passing the signal lepton requirements, with any extra baseline leptons being vetoed. Events are required to have either 2 or 3 jets with transverse momentum greater than 25 GeV, and exactly two jets being b-tagged using the MV2c10 algorithm. The b-tagged jets are also required to have transverse momentum greater than 25 GeV. Lower bound requirements are placed on the m_{bb} and m_{T} variables to reduce the combinatoric and multi-jet backgrounds. Finally, all events are required to pass one of the $E_{\mathrm{T}}^{\mathrm{miss}}$ triggers detailed in Section **??**.

Variable	Selection
$N_{\ell}^{\mathrm{baseline}}$	$= 1$
$N_{\ell}^{\mathrm{signal}}$	$= 1$
$p_{\mathrm{T}}(\ell_1)$	> 27 GeV
N_{jet}	$= 2$ or 3
$p_{\mathrm{T}}(\mathrm{jet})$	> 25 GeV
$N_{b-\mathrm{jet}}$	$= 2$
$p_{\mathrm{T}}(b-\mathrm{jet})$	> 25 GeV
m_{T}	> 40 GeV
m_{bb}	> 50 GeV

Table 1.1: A summary of the preliminary event selection used in the 36.1fb^{-1} search for $\tilde{\chi}_1^{\pm}\tilde{\chi}_2^0$ pair-production.

At the preselection level, the dominant SM backgrounds are $t\bar{t}$, Wt-channel single top and W+jets. Three SRs are defined, each targeting a different region of the m($\tilde{\chi}_1^{\pm}/\tilde{\chi}_2^0$)-m($\tilde{\chi}_1^0$) parameter space. SRLM is optimised to target scenarios where the mass-splitting of the m($\tilde{\chi}_1^{\pm}/\tilde{\chi}_2^0$) and m($\tilde{\chi}_1^0$), denoted by $\Delta\mathrm{M}(\tilde{\chi}_1^{\pm}/\tilde{\chi}_2^0, \tilde{\chi}_1^0)$, is similar to the Higgs mass. SRMM and SRHM target larger $\Delta\mathrm{M}(\tilde{\chi}_1^{\pm}/\tilde{\chi}_2^0, \tilde{\chi}_1^0)$, around 150-250 GeV and > 250 GeV, respectively. The variables identified to separate the signal from the SM backgrounds were the $E_{\mathrm{T}}^{\mathrm{miss}}$, m_{T}, m_{bb} and m_{CT}. Each of these variables are described in Section **??**. The three SRs are defined in Table 1.2.

	SRLM	SRMM	SRHM
m_{bb}	$\in [105, 135]$ GeV		
m_{CT}	> 160 GeV		
$E_{\mathrm{T}}^{\mathrm{miss}}$	> 200 GeV		
m_{T}	$\in [100, 140]$ GeV	$\in [140, 200]$ GeV	> 200 GeV

Table 1.2: A summary of the signal region selections used in the SUSY Wh $1\ell + b\bar{b} + E_{\mathrm{T}}^{\mathrm{miss}}$ analysis.

The invariant mass of the two b-jets, m_{bb}, targets the Higgs boson mass, selecting events in the range $105 < m_{bb} < 135$ GeV. The contranservse mass, m_{CT}, is required to satisfy $m_{\mathrm{CT}} > 160$ GeV, to effectively suppress the $t\bar{t}$ process. The transverse mass, m_{T}, is required to be greater than 100 GeV to suppress the W+jets background, with three bins defined to target different $\Delta\mathrm{M}(\tilde{\chi}_1^{\pm}/\tilde{\chi}_2^0, \tilde{\chi}_1^0)$ scenarios.

1.3 Background estimation

The $t\bar{t}$, single top and W+jets backgrounds are the most dominant backgrounds in the three SRs. Each of these major backgrounds have corresponding CRs defined in which to evaluate the process-specific normalisations, μ_{process}. The $t\bar{t}$ CR is defined with 3 m_{T} bins, matching the m_{T} ranges of the 3 SR bins, named CR($t\bar{t}$)-LM, CR($t\bar{t}$)-MM and CR($t\bar{t}$)-HM, respectively. The top-pair CRs invert the selection on the m_{CT} variable described in Chapter **??** to target the production of a pair of top quarks, while the selection on m_{bb} is inverted as the distribution is not expected to peak around the Higgs masses. A single-bin CR for the single top background, CR(t), and a single-bin CR for the W+jets background, CR(W), are also defined. The single-top CR is defined by requiring the m_{bb} is large to target the presence of b-quarks coming from the decay of a top quark and the initial state gluon splitting. Finally, the W+jets CR exploits the m_{T} variable, as described in Chapter **??**, to target the decay of a single leptonic W boson, while rejecting the $t\bar{t}$ background. The full definitions of these regions are given in Table 1.3.

	Region				
Variable	CR($t\bar{t}$-LM)	CR($t\bar{t}$-MM)	CR($t\bar{t}$-HM)	CR(t)	CR(W)
m_{T} [GeV]	$\in [100, 140]$	$\in [140, 200]$	> 200	> 100	$\in [40, 100]$
m_{CT} [GeV]	< 160	< 160	< 160	> 160	> 160
m_{bb} [GeV]	$\notin [105, 135]$	$\notin [105, 135]$	$\notin [105, 135]$	> 195	< 80
$E_{\mathrm{T}}^{\mathrm{miss}}$ [GeV]	> 200	> 200	> 200	> 200	> 200

Table 1.3: Control region definitions for the SUSY Wh $1\ell + b\bar{b} + E_{\mathrm{T}}^{\mathrm{miss}}$ analysis.

Six VRs are defined, three targeting m_{bb} values in a window around the Higgs peak, $m_{\mathrm{bb}} \in [105, 135]$ GeV, with three further VRs targeting m_{bb} values in the sideband region. The former VRs are referred to as 'on-peak' regions, denoted by $\mathrm{VR_{on}}$, while the latter are referred to as 'off-peak' regions and are denoted by $\mathrm{VR_{off}}$. Each set of VRs mirrors the SR binning in the m_{T} variable. The explicit VR definitions are given in Table 1.4.

	Region		
Variable	$\mathrm{VR_{on}}$(LM)	$\mathrm{VR_{on}}$(MM)	$\mathrm{VR_{on}}$(HM)
m_{T} [GeV]	$\in [100, 140]$	$\in [140, 200]$	> 200
m_{CT} [GeV]	< 160	< 160	< 160
m_{bb} [GeV]	$\in [105, 135]$	$\in [105, 135]$	$\in [105, 135]$
$E_{\mathrm{T}}^{\mathrm{miss}}$ [GeV]	> 200	> 200	> 200
	Region		
Variable	$\mathrm{VR_{off}}$(LM)	$\mathrm{VR_{off}}$(MM)	$\mathrm{VR_{off}}$(HM)
m_{T} [GeV]	$\in [100, 140]$	$\in [140, 200]$	> 200
m_{CT} [GeV]	> 160	> 160	> 160
m_{bb} [GeV]	$< 95 \,\|\|\, \in [145, 195]$		
$E_{\mathrm{T}}^{\mathrm{miss}}$ [GeV]	> 180	> 180	> 180

Table 1.4: Validation region definitions for the SUSY Wh $1\ell + b\bar{b} + E_{\mathrm{T}}^{\mathrm{miss}}$ analysis. The subscript 'on' and 'off' refer respectively to the m_{bb} requirement targeting the Higgs boson, hence 'on-peak', and targeting the sideband regions, or 'off-peak'.

1.4 Systematic uncertainties

Three sources of uncertainty are considered in this analysis; statistical uncertainties, arising from the finite statistics in both data and the MC, experimental systematics and modelling systematics. Section **??** describes the experimental systematics evaluated, along with the transfer factor prescription which is used to evaluate the modelling uncertainties in this analysis.

The dominant experimental systematics originate from the JER, totalling upto 20% of the background uncertainty in SRMM, with the subdominant experimental systematics arising from the b-tagging uncertainties. The dominant theory uncertainties arise from the modelling of the $t\bar{t}$ process, ranging from 15-20% of the total background uncertainty in the SRs. The uncertainty due to the interference between the Wt-channel single top and $t\bar{t}$ processes ranges from 30% to 52% on the single top estimate in the SRs.

$1\ell + b\bar{b} + E_{\mathrm{T}}^{\mathrm{miss}}$ **channel**			
Uncertainty of region	SRLM	SRMM	SRHM
Total background expectation	5.7	2.8	4.6
Total background uncertainty	±2.3	±1.0	±1.2
Systematic, experimental	±1.3	±0.7	±0.6
Systematic, theoretical	±2.2	±0.9	±0.7
Statistical, MC samples	±1.1	±0.5	±0.6
Statistical, $\mu_{\mathrm{TT,ST,Wj}}$ scale-factors	±0.8	±0.6	±1.3

Table 1.5: Table showing a summary of the experimental and modelling uncertainties in the SUSY Wh $1\ell + b\bar{b} + E_{\mathrm{T}}^{\mathrm{miss}}$ analysis.

1.5 Results

Background-only fit results

The results of the background-only fit in the CRs and SRs for the $1\ell + b\bar{b}$+$E_{\mathrm{T}}^{\mathrm{miss}}$ channel are shown in Tables 1.6 and 1.7, respectively. As explained in Chapter **??**, the background-only fit configuration uses only the CRs to normalise the dominant backgrounds, in this case $t\bar{t}$, single top and W+jets. The $t\bar{t}$ background has 3 separate normalisation factors, one for each m_{T} bin, such that data/MC differences in each region can be corrected independently of each other. The results of the background-only fit are then extrapolated to the VRs and SRs, such that an estimate of the backgrounds in the SR can be derived without bias from any potential excesses in the SRs, or assumptions on the signal model itself. Excellent data/SM agreement is observed in the CRs and most of the VRs. In $\mathrm{VR_{on}}$-HM and SRMM, there are excesses between $1.5 - 2\sigma$.

The normalisation factors derived for the $t\bar{t}$, single top and W+jets backgrounds using the background-only fit configuration are given in Table 1.8, showing all values are compatible with unity.

Post-fit distributions in the CRs are shown in Figure **??**, where excellent data/SM agreement is observed. The uncertainty band in the ratio includes all statistical and systematic uncertainties on the SM backgrounds. Figure 1.4 shows the data/SM agreement in the VRs, where good agreement is observed within 2σ.

Control regions	CR($t\bar{t}$)-LM	CR($t\bar{t}$)-MM	CR($t\bar{t}$)-HM	CR(W)	CR(t)
Observed events	192	359	1115	72	65
Fitted bkg events	192 ± 14	359 ± 19	1115 ± 34	72 ± 9	65 ± 8
$t\bar{t}$	147 ± 33	325 ± 32	1020 ± 90	15 ± 14	20^{+23}_{-20}
Single top	28 ± 25	22^{+24}_{-22}	60^{+70}_{-60}	4^{+6}_{-4}	33 ± 25
W+jets	16 ± 7	7.3 ± 2.7	25 ± 11	51 ± 17	8 ± 4
t$\bar{\text{t}}$V	1.16 ± 0.20	2.8 ± 0.4	6.9 ± 1.1	0.079 ± 0.022	3.2 ± 0.6
Diboson	0.57 ± 0.24	0.92 ± 0.29	1.3 ± 0.4	2.1 ± 1.1	0.84 ± 0.28
Others	0.125 ± 0.032	0.20 ± 0.06	1.9 ± 0.5	0.24 ± 0.17	0.10 ± 0.04

Table 1.6: Table showing the results of the background-only fit in the CRs of the SUSY Wh $1\ell + b\bar{b} + E_{\text{T}}^{\text{miss}}$ analysis. Excellent data/SM agreement is observed in all regions.

Signal regions	SRLM	SRMM	SRHM
Observed events	6	7	5
Fitted bkg events	5.7 ± 2.3	2.8 ± 1.0	4.6 ± 1.2
$t\bar{t}$	3.4 ± 2.9	1.4 ± 1.0	1.1 ± 0.6
Single top (Wt)	$1.4^{+1.4}_{-1.4}$	$0.8^{+0.9}_{-0.8}$	1.2 ± 1.1
W + jets	0.6 ± 0.4	0.20 ± 0.11	1.6 ± 0.6
t$\bar{\text{t}}$V	0.10 ± 0.04	0.32 ± 0.09	0.54 ± 0.14
Diboson	$0.12^{+0.15}_{-0.12}$	0.05 ± 0.03	0.08 ± 0.02
Others	0.10 ± 0.05	0.03 ± 0.01	0.04 ± 0.02

Table 1.7: Table showing the background-only fit results in the SRs of the SUSY Wh $1\ell + b\bar{b} + E_{\text{T}}^{\text{miss}}$ analysis. Excellent data/SM agreement is observed in SRLM and SRHM, while in SRMM there is a small discrepancy of $\sim 2\sigma$ significance.

Background normalisations	
$\mu(t\bar{t}\text{-LM})$	1.02 ± 0.14
$\mu(t\bar{t}\text{-MM})$	1.15 ± 0.13
$\mu(t\bar{t}\text{-HM})$	$0.89^{+0.21}_{-0.20}$
$\mu(W)$	1.40 ± 0.5
$\mu(t)$	$1.10^{+0.7}_{-1.1}$

Table 1.8: Table showing the background normalisation factors for the SUSY Wh $1\ell+b\bar{b}+$ $E_{\mathrm{T}}^{\mathrm{miss}}$ analysis, derived by performing a simultaneous fit of all CRs as described in Section **??**.

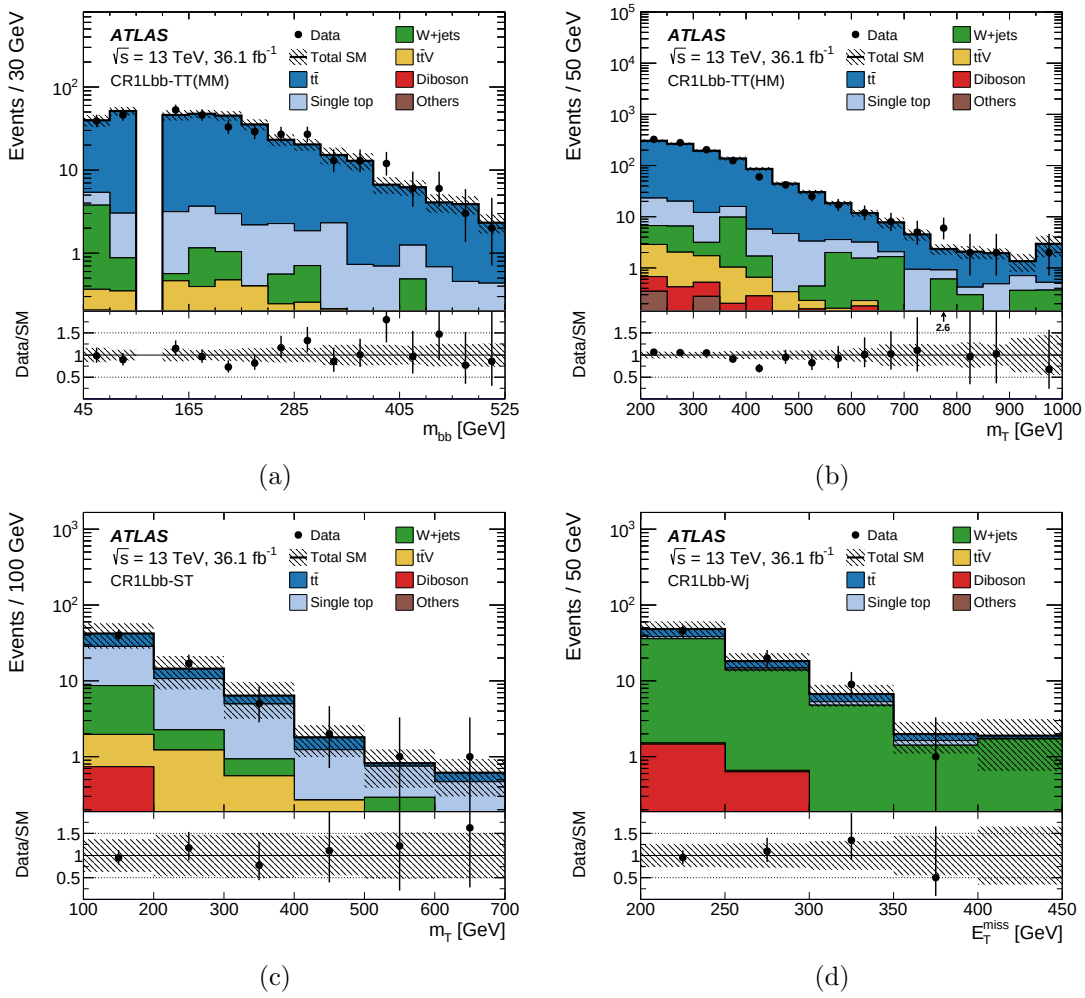

Figure 1.3: Plots showing the post-fit N-1 distributions of the key kinematic variables in the CRs. The uncertainty band in the ratio plots contains MC statistical uncertainties and all systematic uncertainties.

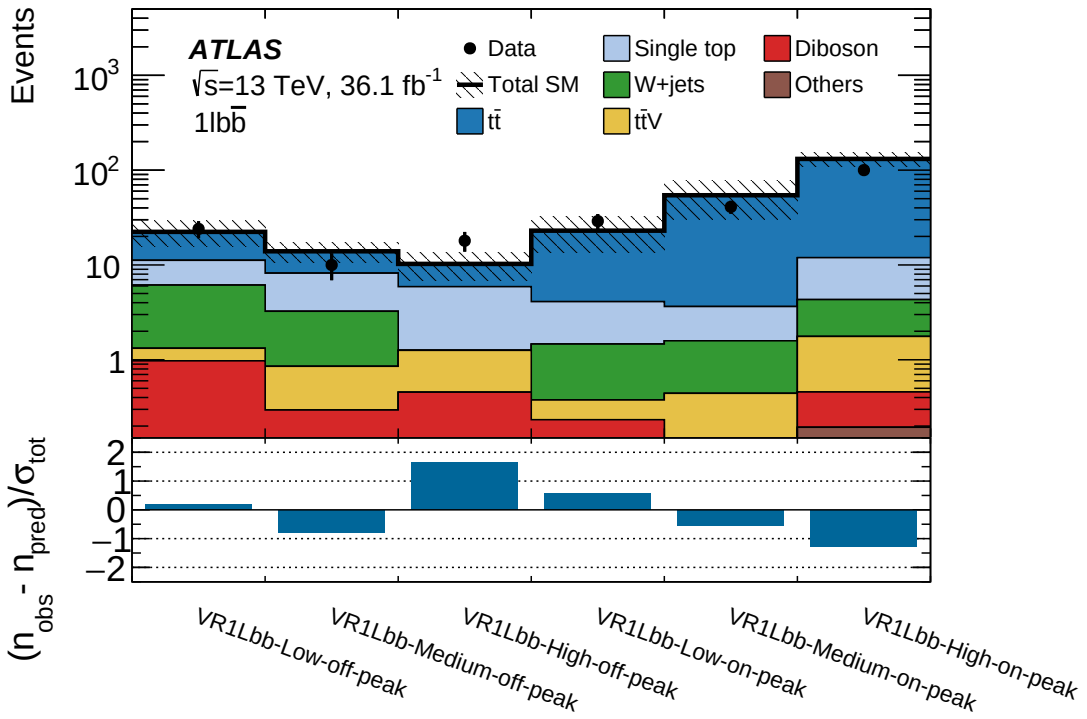

Figure 1.4: Summary plot showing the data/SM agreement in all VRs for SUSY Wh $1\ell + b\bar{b} + E_{\mathrm{T}}^{\mathrm{miss}}$ analysis. The uncertainty used to calculate the significance of the data/SM difference includes the statistical component on the MC and the data, as well as the totalsystematic uncertainty on the background estimate.

Model-dependent results

As shown in the background-only fit results presented previously, no significant excesses are observed in the SRs. In this case, model-dependent exclusion limits are set on $\tilde{\chi}_1^{\pm}\tilde{\chi}_2^0$ pair-production decaying via the Wh signature to the $1\ell+b\bar{b}+E_{\mathrm{T}}^{\mathrm{miss}}$ final state. As described in Section **??**, the model-dependent fit configuration uses both the CRs and SRs to set 95% confidence limits on the presence of a given signal model. The model-dependent exclusion limits for the analysis using a dataset of 36.1fb^{-1} collected at $\sqrt{s} = 13$ TeV is shown in Figure 1.5, excluding $\tilde{\chi}_1^{\pm}/\tilde{\chi}_2^0$ masses upto 550 GeV for a massless $\tilde{\chi}_1^0$.

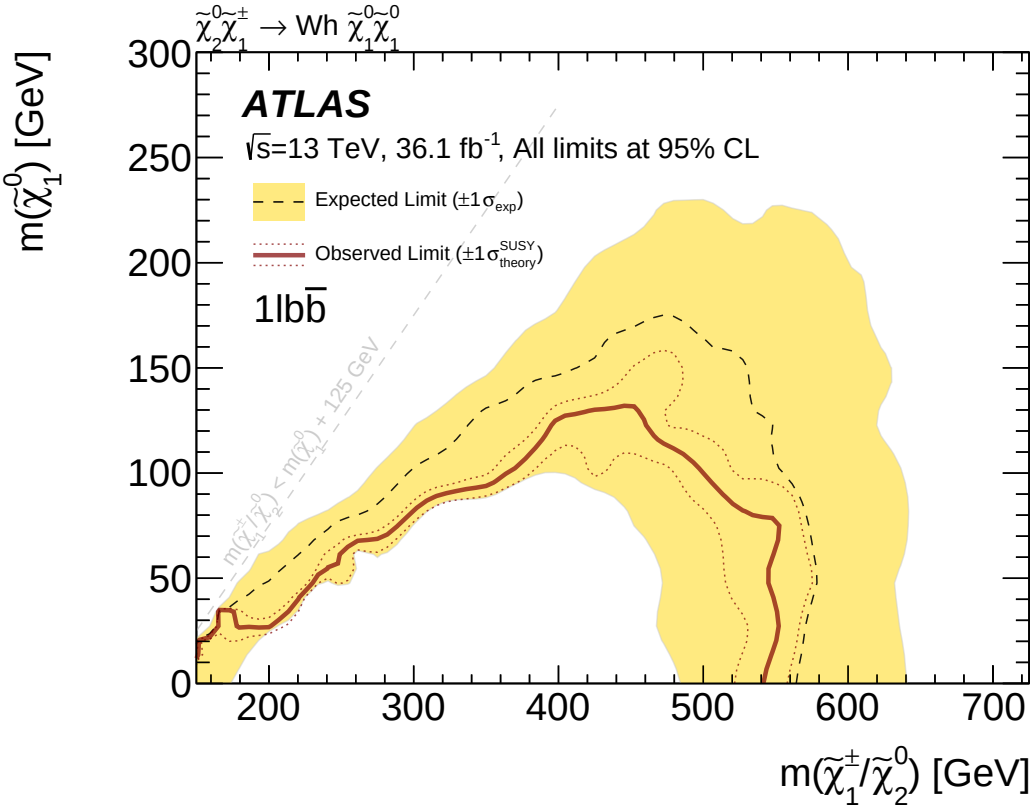

Figure 1.5: Plots showing the sensitivity to $\tilde{\chi}_1^{\pm}\tilde{\chi}_2^0$ pair-production with the Wh signature, decaying via the $1\ell + b\bar{b}+E_{\mathrm{T}}^{\mathrm{miss}}$ channel.

Model-independent limits

In addition to the model-dependent fit, 95% confidence limits are set on a generic BSM process using the model-independent fit strategy detailed in Section **??**. A visible cross-section, σ_{vis}, is derived which represents the product of the signal selection efficiency, ϵ, the detector acceptance, A and the production cross-section for the BSM process, σ_{BSM}. The model-independent limits on σ_{vis} derived using the SRs defined early are shown in Table 1.9, as well as limits on the expected and observed number of signal events.

	σ_{vis} [fb]	S_{obs}^{95}	S_{exp}^{95}	p_0-value
SRLM	0.23	8.3	$8.0^{+3.3}_{-2.2}$	0.46
SRMM	0.28	10.0	$5.6^{+2.9}_{-1.7}$	0.04
SRHM	0.18	6.4	$6.1^{+3.1}_{-1.9}$	0.44

Table 1.9: From left to right, the observed 95% CL upper limits on the visible cross-sections σ_{vis}, the observed (S_{obs}^{95}) and expected (S_{exp}^{95}) 95% CL upper limits on the number of signal events with $\pm 1\sigma$ variations of the expectation, and the discovery p-value (p_0).

As shown in Table 1.9, the upper limit on the visible cross-section for a generic BSM process ranges from 0.18-0.28 fb.

1.6 Studies using 139fb^{-1} data

The search for $\tilde{\chi}_1^{\pm}\tilde{\chi}_2^0$ described previously in this Chapter made use of 36.1 fb^{-1} pp collision data collected by ATLAS at $\sqrt{s} = 13$ TeV. An update to this analysis was performed using the full Run-2 dataset [6], collected between 2015-2018, and using a reoptimisation of the selections described in Table 1.2. ML studies are currently underway to improve the sensitivity to the signal, with some initial studies presented in Section 1.6.

Reoptimised analysis using full Run-2 dataset

With the full Run-2 dataset of 139fb^{-1}, the selections described in Table 1.2 were not sensitive to the signal, due to the relative size difference of the dominant SM background cross-sections to the signal. A reoptimised analysis strategy was developed, making use of multi-bin fits as described in Section **??**, as well as the invariant mass of the lepton and the highest-p$_{\text{T}}$ b-tagged jet, $m(\ell, b_1)$, which is defined as:

$$m(\ell, b_1) = \left((E_{\ell,1} + E_{b,1})^2 - ||\mathbf{p}_{\ell,1} + \mathbf{p}_{b,1}||^2 \right)^{1/2} . \tag{1.6.1}$$

When the lepton and the leading b-jet are both from the decay of a top quark, the $m(\ell, b_1)$ distribution has a kinematic endpoint at $\sqrt{m_t^2 - m_W^2}$, enabling good background rejection for processes with a leptonically-decaying top quark. The full SR definitions are given in Table 1.10. The major difference in the SR definitions of the 36.1fb^{-1} analysis (Table 1.2) and the 139fb^{-1} analysis (Table 1.10) is the binning in the m_{CT} variable. Each of the three SR types, SRLM, SRMM and SRHM, is separated into three bins in m_{CT}. As described in Section **??**, performing a statistical analysis on multiple bins simutaneously can increase the sensitivity to a signal model. The SRs demarcated by *(excl.)* are the SRs used for the model-dependent fit, while the SRs demarcated by *(disc.)* were the 'discovery' SRs used for the model-independent fit. The discovery regions are inclusive in both m_{T} and

	SRLM	SRMM	SRHM
N_{lepton}	$= 1$		
$p_{\text{T}}^{\ell_1}$ [GeV]	$> 7(6)$ for $e(\mu)$		
N_{jet}	$= 2$ or 3		
$N_{b\text{-jet}}$	$= 2$		
$E_{\text{T}}^{\text{miss}}$ [GeV]	> 240		
m_{bb} [GeV]	$\in [100, 140]$		
$m(\ell, b_1)$ [GeV]	–	–	> 120
m_{T} (excl.) [GeV]	$\in [100, 160]$	$\in [160, 240]$	> 240
m_{CT} (excl.) [GeV]	$\{\in [180, 230], \in [230, 280], > 280\}$		
m_{T} (disc.) [GeV]	> 100	> 160	> 240
m_{CT} (disc.) [GeV]	> 180		

Table 1.10: Overview of the selection criteria for the signal regions. Each of the three 'excl.' SRs is binned in three m_{CT} regions for a total of nine 'excl.' bins.

m_{CT} , to remove any assumption about the shape of these distributions for a generic BSM signal. The background estimation strategy is very similar to that defined in Section 1.3. The data/SM agreement in all regions is shown in Figure 1.6, where good agreement is seen in all regions within 2σ. In the absence of a significant excess, exclusion limits are set at 95% CL, as shown in Figure 1.7. As shown in Figure 1.7, $\tilde{\chi}_1^{\pm}/\tilde{\chi}_2^0$ masses upto 740 GeV were excluded by the analysis using a dataset of 139fb^{-1}. The discrepancy between the expected and observed exclusion limits is due to the small overfluctuation of data between $1 - 2\sigma$ in several of the SR bins, as seen in Figure 1.6.

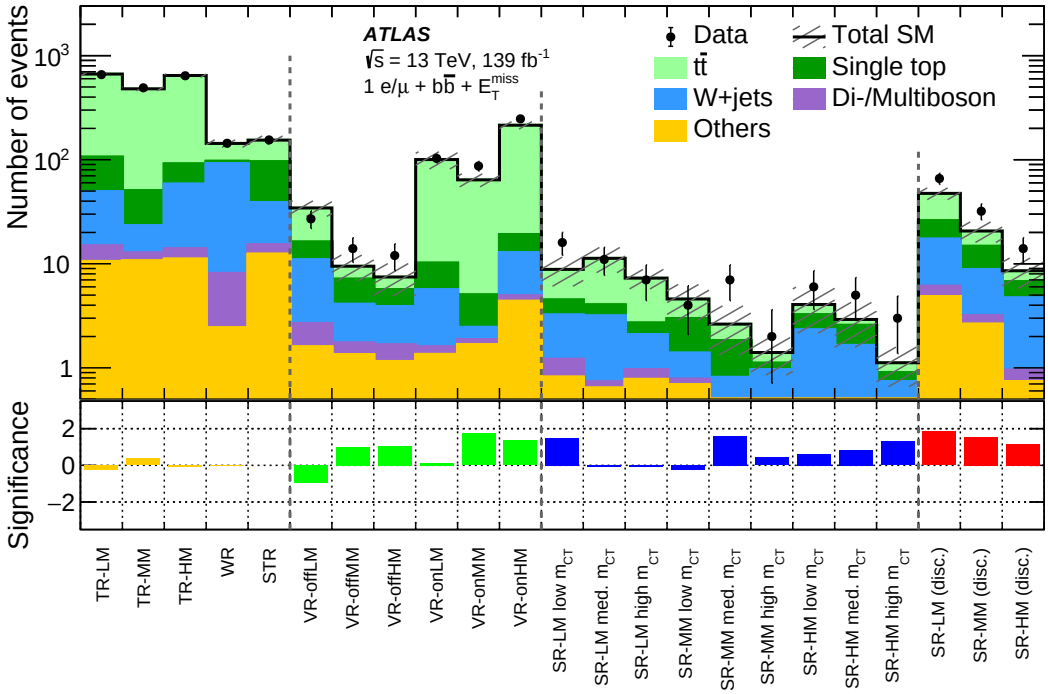

Figure 1.6: Plot showing the data/SM agreement in all CR/VR/SRs for the 139fb^{-1} SUSY Wh $1\ell + b\bar{b} + E_{\mathrm{T}}^{\mathrm{miss}}$ analysis. Good agreement is seen in all regions.

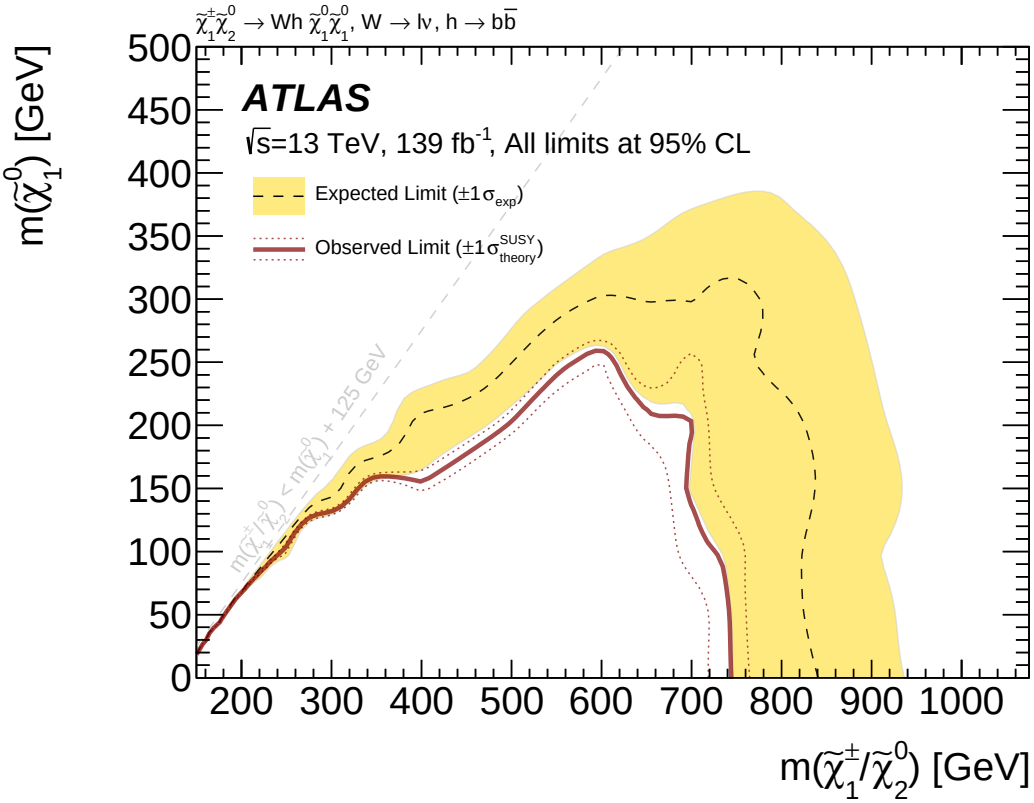

Figure 1.7: 95% CL exclusion limits for the SUSY Wh $1\ell + b\bar{b} + E_{\mathrm{T}}^{\mathrm{miss}}$ analysis, using the full Run-2 dataset of 139fb^{-1}. $\tilde{\chi}_1^{\pm}/\tilde{\chi}_2^0$ masses upto 740 GeV are excluded for a massless $\tilde{\chi}_1^0$.

ML studies

In regions of phase space where the signal and background kinematics are very similar, selecting signals by applying selections to a discriminative variables will generally result in poor sensitivity. In this analysis, the separation of signal and background is particularly challenging in kinematically 'compressed' scenarios, where the mass-splitting of the $\tilde{\chi}_1^{\pm}/\tilde{\chi}_2^0$ and $\tilde{\chi}_1^0$ is small. The use of ML methods to separate kinematically-challenging signal processes from the dominant backgrounds was studied. The use of high-level variables, such as m_{T} and m_{CT}, defined as variables which are calculated using low-level, such as the transverse momenta of the objects, can enable ML classifiers to achieve sensitivity to the signal.

Two ML classifiers were trained to separate the $t\bar{t}$ process, Wt-channel single top process and a compressed benchmark signal model process, with $\mathrm{m}(\tilde{\chi}_1^{\pm}/\tilde{\chi}_2^0) = 400$ GeV and $\mathrm{m}(\tilde{\chi}_1^0) = 250$ GeV. A boosted decision tree and a deep neural network, the general principles of which are described in Chapter **??**, were trained in the multiclass configuration on the following high-level and low-level variables:

- High-level: $E_{\mathrm{T}}^{\mathrm{miss}}$, m_{T}, m_{CT}, m_{bb}, $m(\ell, \mathrm{b}_1)$, $m(\ell, \mathrm{b}_2)$, $\Delta R(\mathrm{b}_1, \mathrm{b}_2)$
- Low-level: $p_{\mathrm{T}}(\ell_1)$, $p_{\mathrm{T}}(b_1)$, $p_{\mathrm{T}}(b_2)$, $\eta(\ell_1)$, $\eta(b_1)$, $\eta(b_2)$

It was found by testing the performance of models including both high-level and low-level variables and comparing to models with only high-level variables that no additional discrimination was achieved when including the low-level variables, and thus they were not included in subsequent trainings. As both ML models were trained as multiclass classifiers, the output of both models is a prediction for each class. In practice, this means there are three values output for each event, corresponding to how $t\bar{t}$-like, how Wt-like and how signal-like each event is.

The receiver operating characteristic (ROC) curve shown in Figure 1.8 shows the signal effiency versus background rejection for the $t\bar{t}$, Wt and signal classes.

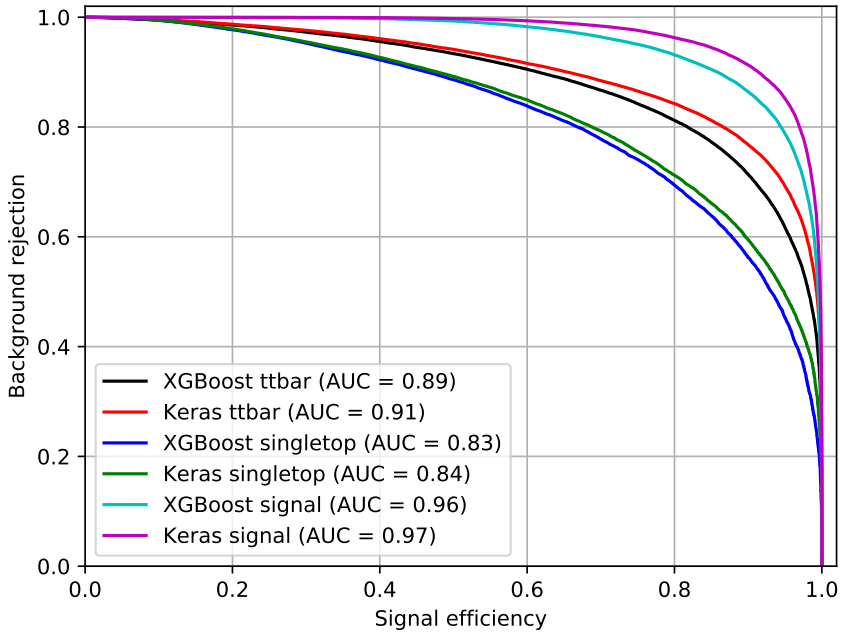

Figure 1.8: ROC curves showing the classification performance of the BDT and DNN for $t\bar{t}$, Wt-channel single top and signal classes.

Each ROC curve is a measure of how well a classifier separates one class from the others. The area under curve (AUC) value is the integral of the ROC curve, and is a measure of the classification accuracy of a model. As can be seen, the classification accuracy for both the BDT and DNN correctly selects signal events versus the background classes most frequently.

The bulk of this work was in developing the ML framework. An analysis using this ML framework is currently under development and will be the subject of another Thesis from the University of Liverpool.

Chapter 2

Search for Dark Matter produced in association with a Top Quark

This Chapter presents a search for the production of Dark Matter (DM) in association with a single top quark, also referred to as DMt, using the full Run-2 dataset collected by ATLAS of 139fb^{-1}. The results of the analysis are interpreted in the context of a simplified model of DM production, where the DM is coupled to an extended SM Higgs sector (2HDM) by a massive, spin-0, pseudoscalar mediator, a.

This Chapter focuses mainly on the $tW+E_{\mathrm{T}}^{\mathrm{miss}}$ signature with a single lepton final state. A complementary analysis of the two lepton final state was also performed, as documented in [7], and will not be detailed here. In addition to the $tW+E_{\mathrm{T}}^{\mathrm{miss}}$ signature, it was found that the sensitivity of these analyses to DM produced in association with a $t\bar{t}$ pair, referred to as DM$t\bar{t}$, was non-negligble. The overall sensitivity of this analysis to the DM$t+t\bar{t}$ signal was evaluted and is detailed in the fit results. Finally, in addition to the independent analyses of the single- and two-lepton final states, both channels were statistically-combined to increase the sensitivity to the DMt and DM$t + t\bar{t}$ signals.

This Chapter begins with a description of the simplfied DM model used to interpret the results, focusing on the experimental signature of interest, the $tW+E_{\mathrm{T}}^{\mathrm{miss}}$ signature. The SR optimisation and selections, as well as the background estimation strategy are documented, before finally presenting the analysis results. Firstly, the background-only fit results in the CRs and SRs are presented, before presenting the model-dependent and model-independent results.

2.1 2HDM+a signal model

As described in Section **??**, there is a strong motivation for performing searches for the production of Dark Matter (DM) at the LHC. Many searches for DM production have already

been carried out using ATLAS data, with the results of the searches being interpreted in the context of the LHC DM simplfied models, as described in [8–10]. These models introduce a new, spin-0 pseudoscalar mediator which couples the SM to DM. However, such models have a limited phenomenology [11], and examples of these models violating gauge invariance and unitarity have also studied [12]. Therefore, while the DM simplified models serve as an excellent benchmark in searches for DM production, a more complete and theoretically-consistent description of DM production is needed.

The simplest extension to the LHC DM simplified models adds a second Higgs doublet to the SM (2HDM). This enables the mixing of the spin-0 mediator with the SM, while also not violating constraints set on the SM Higgs couplings. The particular model of interest in this thesis is the case of a 2HDM model, with an additional pseudoscalar mediator, a. For this model, the $tW+E_{\mathrm{T}}^{\mathrm{miss}}$ signature has not been previously studied, but has been shown to have promising potential in sensitivity studies [11]. The dominant Feynman diagrams for this signature are shown in Figure 2.1. The diagram shown in Figure 2.1a is present in the LHC DM simplified models, while the diagram shown in Figure 2.1b is only present in the 2HDM+a model. The latter diagram gives an approximate order-of-magnitude enhancement to the $pp \to tW\chi\chi$ cross-section through the on-shell production of the charged Higgs, H^-. The additional diagrams from the 2HDM+a model also interfere destructively with the diagrams from the LHC DM simplified model, restoring unitarity.

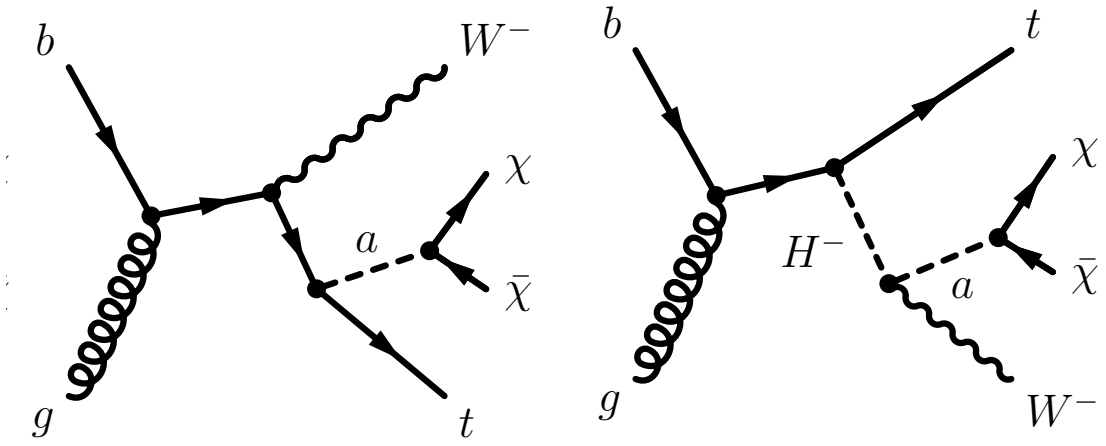

(a) (b)

Figure 2.1: Feynman diagram for dark matter production in the Wt channel, in the context of a 2HDM+a model. This chapter documents studies done in the single lepton channel, where one of the W bosons in the event decays leptonically.

In addition to the $tW+E_{\mathrm{T}}^{\mathrm{miss}}$ signature, the analysis described in the later sections of this Chapter is also sensitive to the $t\bar{t}+E_{\mathrm{T}}^{\mathrm{miss}}$ signature of associated DM production. A rescaling procedure is applied to the DM$t\bar{t}$ process, which is generated, using the DMSimp

framework [13], in the context of a simplified DM production model in which the pseudoscalar mediator a directly couples to the SM. The Feynman diagram for this process is shown in Figure 2.2. The predictions of this simplified model are rescaled to correctly model the prediction using the 2HDM+a model using the procedure described in [14], which also includes contributions from the heavy pseudoscalar A.

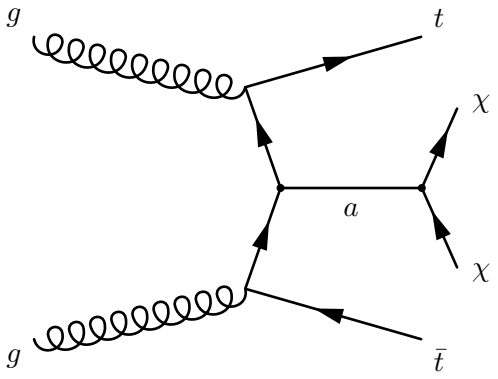

Figure 2.2: Diagram of DM produced in association with a $t\bar{t}$ pair, in the context of the 2HDM+a model under study in this Chapter. The sensitivity of the analysis described later in this Chapter to this signal is shown in Section 2.5.

The model under study in this Chapter is described in detail in [14], but an overview of the most prominent parameters and the choices assigned is given here. As previously described in Section **??**, models with a second Higgs doublet comprise five physical states; the CP-even scalars h and H, the CP-odd pseudoscalar A, and two charged Higgs bosons $H^{\pm}$. The coupling of the extended Higgs sector is of Type-II, such that one Higgs doublet couples to up-type fermions while the other couples to down-type fermions. The mixing in the extended Higgs sector is specified by three mixing angles, α, θ and β. α represents the mixing angle of the two CP-even states, θ represents the mixing of the CP-odd states, and $\tan\beta$ represents the ratio of the VEVS of the two Higgs doublets. The *alignment limit* is assumed, where $\cos(\beta-\alpha)=0$, such that h can be identified with the SM Higgs boson. To enhance the sensitivity to this model, it is assumed that there is maximal mixing between the Higgs sector and the mediator, A and a, and as such it is assumed that $\sin\theta = 1/\sqrt{2}$. As described in [14], it is assumed the masses of the CP-even neutral Higgs, the CP-odd Higgs and the charged Higgs states are degenerate, and the mass of the DM, m_{χ} is set equal to 10 GeV. Finally, the DM coupling to a is set equal to unity, $y_{\chi}=1$. Therefore, there are three free parameters; $\tan\beta$, $m_{H^{\pm}}$ and m_a. In order to set model-dependent limits on this process, two planes are defined to cover the largest possible region of the available model phase space. The first is a scan in the $m_a, m_{H^{\pm}}$ plane, assuming $\tan\beta=1$, while the second plane is a scan in the $m_{H^{\pm}}, \tan\beta$ plane, assuming $m_a = 250$ GeV. The cross-section dependence on $\tan\beta$ for the DMt and DM$t\bar{t}$ processes is shown in Figure 2.3, with $m_a = 250$ GeV and $m_{H^{\pm}} = 600$ GeV. As seen, the cross-section for the DM$t\bar{t}$ process has a $1/\tan^2\beta$ dependence, while the DMt has a more complex dependence on the value of

282 $\tan\beta$. A summary of the model parameter choices is given in Table 2.1.

Fixed parameters	Assumption
$\sin\theta$	$= 1/\sqrt{2}$
$\cos(\beta - \alpha)$	$= 0$
m_h	$= 125$ GeV
m_H, m_A, $m_{H\pm}$	Degenerate
m_χ	$= 10$ GeV
y_χ	$= 1$

Table 2.1: A table summarising the model parameter assumptions for the simplified 2HDM+a model of DM production as described in [14].

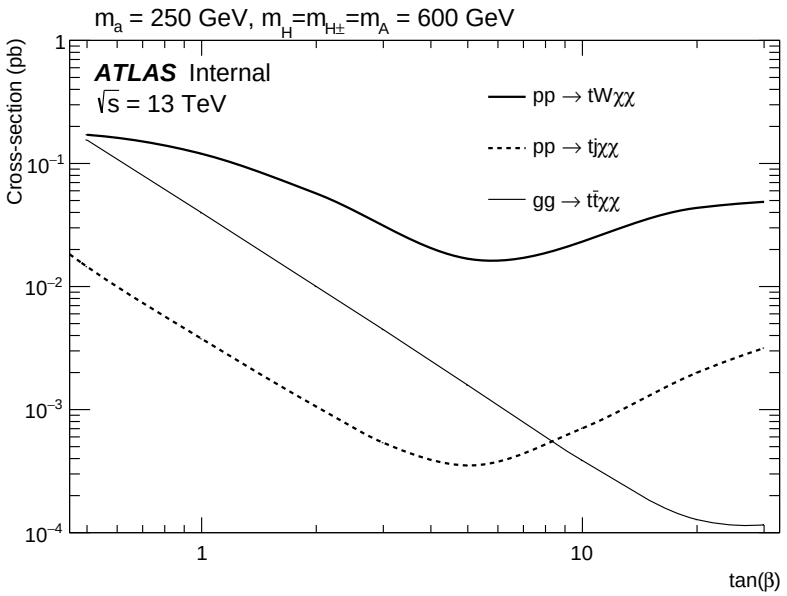

Figure 2.3: Diagram showing the production cross-section of DM produced in association with tW, t and $t\bar{t}$. The associated $t\bar{t}$ production cross-section is proportional to $1/\tan^2\beta$ as described in [15].

283 2.2 Event selection

284 The event selection for this analysis begins with a set of preliminary, loose selections, known
285 as 'preselection'. The preselection cuts aim to select events matching the signal topology,
286 while rejecting events with different topologies. All events are required to have exactly
287 1 electron or muon in the final state, with any additional reconstructed leptons failing
288 the 'signal' lepton requirements being rejected. At least three jets are required, to target
289 events with at least one hadronically-decaying W boson, and at least one b-tagged jet is

required to select events with a top quark. To minimise the background contribution from $t\bar{t}$, events with a second b-tagged jet required it has a transverse momentum $p_{\mathrm{T}}(b_2) < 50$ GeV. The jets and $E_{\mathrm{T}}^{\mathrm{miss}}$ must have an angular separation of at least 0.5 rad, to reject events which have mismeasured jets. All events are required to pass the event cleaning procedure described in Section **??**, as well as passing one of the $E_{\mathrm{T}}^{\mathrm{miss}}$ triggers as described in Section **??**. In order to ensure a constant $E_{\mathrm{T}}^{\mathrm{miss}}$ trigger efficiency, all events are required to have $E_{\mathrm{T}}^{\mathrm{miss}} > 250$ GeV. The full preselection requirements for this analysis are defined in Table 2.2. The definitions for the objects used in this analysis are described in Chapter **??**.

Variable	Selection
$N_{\ell}^{\mathrm{baseline}}$	$= 1$
$N_{\ell}^{\mathrm{signal}}$	$= 1$
$p_{\mathrm{T}}(\ell_1)$	> 30 GeV
N_{jet}	≥ 3
$p_{\mathrm{T}}(jet)$	> 30 GeV
$N_{b-\mathrm{jet}}$	≥ 1
$p_{\mathrm{T}}(b-\mathrm{jet})$	> 50 GeV
$E_{\mathrm{T}}^{\mathrm{miss}}$	> 250 GeV
m_{T}	> 30 GeV
$\lvert\Delta\phi\rvert$	> 0.5 [rad]

Table 2.2: Preliminary selections used for the tW+$E_{\mathrm{T}}^{\mathrm{miss}}$ analysis. All events are also required to pass the $E_{\mathrm{T}}^{\mathrm{miss}}$ trigger, and the event cleaning requirements detailed in Section **??**.The object definitions used are detailed in Chapter **??**.

At the preselection-level, the dominant backgrounds, estimated from MC-only, are $t\bar{t}$ (67%), W+jets (18%) and single top production (11%), where the percentages in parenthesis represents the contribution of that process to the total background. Four key variables were identified which enabled rejection of the backgrounds while maintaining a reasonably high signal selection efficiency; $E_{\mathrm{T}}^{\mathrm{miss}}$, m_{T}, am_{T2} and $m_{\mathrm{W}}^{\mathrm{had}}$. These variables are defined in Section **??**. The am_{T2}, $m_{\mathrm{T}}$and $m_{\mathrm{W}}^{\mathrm{had}}$variables formed the inputs to simultaneous adaptive random grid search and genetic algorithms, as described in Section **??**. The SR selections are summarised in Table 2.3.

2.3 Background estimation

The major backgrounds in the E_T^{miss} bins of the SR vary, depending on bin, between $t\bar{t}$ and W+jets, with smaller contributions from Wt-channel single top production, $t\bar{t}+V$ and the diboson backgrounds. A single-bin CR for the $t\bar{t}$ background, CR($t\bar{t}$) and a 2-bin CR for the W+jets background, CR(W), are defined. For the W+jets background, the CR is

Variable	$\mathrm{SR}_{1\mathrm{L}}^{\mathrm{Bin0}}$	$\mathrm{SR}_{1\mathrm{L}}^{\mathrm{Bin1}}$	$\mathrm{SR}_{1\mathrm{L}}^{\mathrm{Bin2}}$	$\mathrm{SR}_{1\mathrm{L}}^{\mathrm{Bin3}}$	$\mathrm{SR}_{1\mathrm{L}}^{\mathrm{Bin4}}$
$p_{\mathrm{T}}(b_2)$ [GeV]	< 50	< 50	< 50	< 50	< 50
m_{T} [GeV]	> 200	> 200	> 200	> 200	> 200
am_{T2} [GeV]	> 220	> 220	> 220	> 220	> 220
$m_{\mathrm{W}}^{\mathrm{had}}$ [GeV]	> 60	> 60	> 60	> 60	> 60
$E_{\mathrm{T}}^{\mathrm{miss}}$ [GeV]	$\in [250, 300]$	$\in [300, 400]$	$\in [400, 500]$	$\in [500, 600]$	> 600

Table 2.3: Signal region definitions for the tW+$E_{\mathrm{T}}^{\mathrm{miss}}$ analysis.

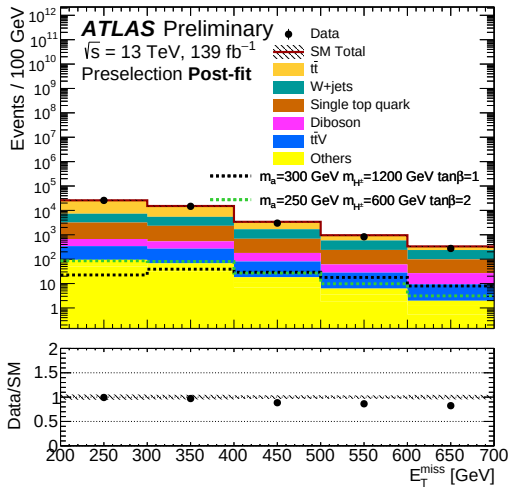

(a) $E_{\mathrm{T}}^{\mathrm{miss}}$

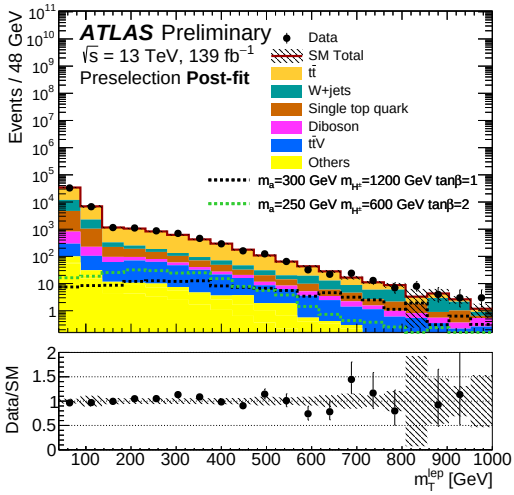

(b) m_{T}

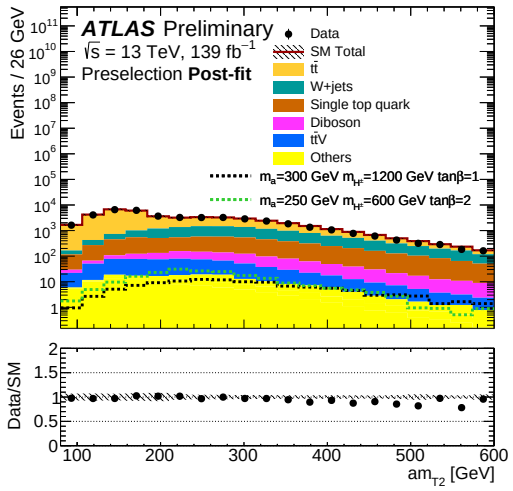

(c) am_{T2}

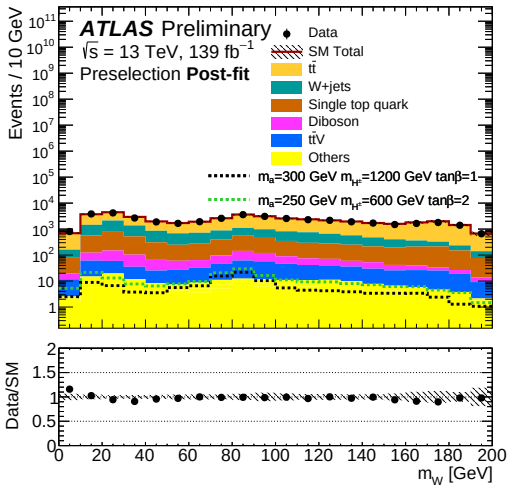

(d) $m_{\mathrm{W}}^{\mathrm{had}}$

Figure 2.4: Post-fit plots of the key kinematic variables. The uncertainty band in the ratio plot contains only the MC statistical uncertainty and the experimental uncertainties.

separated into 2 bins of lepton charge to exploit the charge asymmetry of $W^{\pm}$ production. The definitions of the CRs are given in Table 2.4.

Variable	CR($t\bar{t}$)	CR(W)
N_{ℓ}^{signal}	$= 1$	
$p_{\text{T}}(b_1)$ [GeV]	> 50	
$p_{\text{T}}(b_2)$ [GeV]	> 50	< 50
$E_{\text{T}}^{\text{miss}}$ [GeV]	> 250	
am_{T2} [GeV]	< 220	> 220
m_{T} [GeV]	> 200	$\in [40, 100]$
$m_{\text{W}}^{\text{had}}$ [GeV]	$-$	< 60

Table 2.4: Control region definitions for the tW+$E_{\text{T}}^{\text{miss}}$ analysis. The W+jets CR is split into two bins of lepton charge, such that the $W^{\pm}$ production charge asymmetry can be exploited.

6 validation regions are defined which are in a region of kinematic phase space that is between the CRs and SRs. Two $t\bar{t}$ VRs are defined in order to validate the extrapolation of am_{T2} and m_W, while for the W+jets background, two VRs are defined to validate the extrapolation of m_T and m_W. Each of the W+jets VRs is split into two bins of lepton charge to mirror the CR definition. The VR definitions are explicitly defined in Table 2.5.

Variable	VR1($t\bar{t}$)	VR2($t\bar{t}$)	VR1(W)	VR2(W)
N_{ℓ}^{signal}	$= 1$			
$p_{\text{T}}(b_2)$ [GeV]	< 50			
$E_{\text{T}}^{\text{miss}}$ [GeV]	> 250			
am_{T2} [GeV]	< 220	> 220	> 220	> 220
m_{T} [GeV]	> 200	> 200	$\in [40, 100]$	> 100
$m_{\text{W}}^{\text{had}}$ [GeV]	$-$	< 60	> 60	< 60

Table 2.5: Validation region definitions for the tW+$E_{\text{T}}^{\text{miss}}$ analysis. The W+jets VRs, like the CR, are each split into two bins of lepton charge.

2.4 Systematic uncertainties

In addition to statistical uncertainties in the MC and on data, systematic uncertainties are evaluated on all MC background and signal samples, from both experimental and modelling sources. The experimental systematics considered are described in Section **??**. The dominant experimental systematics in the SRs are from the JES, JER and b-tagging efficiency systematics. The modelling uncertainties on the $t\bar{t}$ and single top backgrounds are the dominant modelling systematics in the SRs. The impact of the choice of the hard-scattering

generator for the $t\bar{t}$ and single-top backgrounds is evaluated by comparing the `Powheg-Box` nominal prediction with `MadGraph5_aMC@NLO`, both interfaced to `Pythia8`. To assess the impact of the PS and hadronisation modelling, the nominal `Powheg+Pythia8`configuration is compared with the nominal hard-scatter generator configuration interfaced to `Herwig7`. As previously described in Section **??**, the uncertainty due to the modelling of the interference between the $t\bar{t}$ and Wt processes is evaluated by comparing the DR and DS schemes, with the derived uncertainty applied to the nominal Wt prediction. The uncertainty due to the choice of renormalisation and factorisation scales, as well as the ISR and FSR parameters are varied using internal weights in the nominal sample. Table 2.6 gives an overview of the size of the dominant systematics in this analysis.

Uncertainty of region	SR_{1L}^{Bin0}	SR_{1L}^{Bin1}	SR_{1L}^{Bin2}	SR_{1L}^{Bin3}	SR_{1L}^{Bin4}
Total background expectation	169.1	171.3	54.7	20.2	15.6
Total background uncertainty	14.0	13.3	6.1	2.8	2.8
Systematic, experimental	6.6	2.6	1.24	0.7	0.4
Systematic, theoretical	4.5	7.3	3.4	1.06	1.12
Statistical, MC samples	4.1	4.1	2.3	1.1	1.2
Statistical, μ scale-factors	8.1	6.7	1.6	0.4	0.3

Table 2.6: Table showing a summary of the dominant experimental and modelling uncertainties.

2.5 Results

Background-only fit results

The background-only fit results in the CRs, VRs and SR bins for the single lepton channel are shown in Tables 2.7, 2.8 and 2.9, respectively. In this configuration, only the CRs enter the fit, allowing an estimate of the backgrounds in the VRs and SRs without any signal assumptions. Generally, excellent data/MC agreement is observed in the CRs and VRs, while in the SRs there are $\sim 1\sigma$ excesses in bins 0 and 1 and an $\sim 1\sigma$ underfluctuation of data in bin 4.

The background normalisation factors for the $t\bar{t}$ and W+jets backgrounds, which are derived in the CRs, are shown in Table 2.10. These show excellent compatibility with the SM, agreeing with unity within 1σ.

Figures 2.5, 2.6 and 2.7 show the key kinematic variables for the CRs, VRs and SRs, respectively, including background normalisation factors from the background-only fit. Good modelling is seen in these variables.

Control regions	CR($t\bar{t}$)	CR(W^+)	CR(W^-)
Observed events	911	3143	1653
Fitted bkg events	907.41 ± 30.52	3135.45 ± 56.87	1665.08 ± 37.50
$t\bar{t}$	846.96 ± 34.11	748.75 ± 83.42	720.78 ± 86.33
Single top	19.82 ± 11.53	276.59 ± 69.50	257.00 ± 70.15
W+jets	3.18 ± 0.75	2005.00 ± 98.23	625.41 ± 42.11
Z+jets	$0.13^{+0.16}_{-0.13}$	6.63 ± 0.99	8.39 ± 1.29
Diboson	0.87 ± 0.25	88.85 ± 15.55	46.05 ± 8.01
$t\bar{t}V$	31.01 ± 7.12	8.16 ± 2.69	5.96 ± 1.52
$t\bar{t}H$	4.37 ± 0.41	1.12 ± 0.17	1.17 ± 0.11
tWZ	1.07 ± 0.29	0.36 ± 0.13	0.32 ± 0.11

Table 2.7: Results of the background-only fit in the control regions for the single lepton channel of the search targeting the 2HDM+a tW+$E_{\mathrm{T}}^{\mathrm{miss}}$ signature. This fit includes only the control regions used to normalise the $t\bar{t}$ and W+jets backgrounds.

Validation regions	VR1($t\bar{t}$)	VR2($t\bar{t}$)	VR1(W^+)	VR1(W^-)	VR2(W^+)	VR2(W^-)
Observed events	1389	482	6127	4479	651	464
Fitted bkg events	1394.19 ± 87.29	463.79 ± 33.54	6721.98 ± 451.82	5025.60 ± 440.57	613.26 ± 69.87	475.28 ± 49.85
$t\bar{t}$	1221.12 ± 70.15	282.62 ± 28.47	3644.44 ± 331.57	3570.86 ± 354.94	282.17 ± 40.09	285.73 ± 41.18
Single top	$53.19^{+59.36}_{-53.19}$	56.98 ± 24.51	626.01 ± 280.23	612.94 ± 274.02	71.09 ± 36.09	73.39 ± 38.19
W+jets	39.07 ± 8.23	68.62 ± 11.94	2245.29 ± 131.23	719.06 ± 48.51	203.16 ± 42.05	70.12 ± 12.03
Z+jets	3.97 ± 2.14	2.67 ± 0.46	7.66 ± 1.05	7.33 ± 1.00	3.56 ± 0.93	2.38 ± 0.39
Diboson	15.29 ± 3.21	27.15 ± 5.48	160.21 ± 28.44	85.60 ± 15.61	34.51 ± 7.06	25.89 ± 5.81
$t\bar{t}V$	54.42 ± 12.05	22.54 ± 5.03	32.39 ± 2.79	23.86 ± 3.07	16.34 ± 3.79	15.27 ± 3.53
$t\bar{t}H$	3.57 ± 0.27	0.71 ± 0.04	4.48 ± 0.33	4.37 ± 0.43	0.69 ± 0.03	0.71 ± 0.05
tWZ	3.56 ± 0.82	2.50 ± 0.62	1.51 ± 0.17	1.58 ± 0.22	1.72 ± 0.44	1.79 ± 0.46

Table 2.8: Results of the background-only fit in the validation regions for the single lepton channel of the search targeting the 2HDM+a tW+$E_{\mathrm{T}}^{\mathrm{miss}}$ signature. This fit includes only the control regions used to normalise the $t\bar{t}$ and W+jets backgrounds.

Signal regions	SR1LBin0	SR1LBin1	SR1LBin2	SR1LBin3	SR1LBin4
Observed events	182	191	60	24	12
Fitted bkg events	169.12 ± 13.98	171.28 ± 13.34	54.70 ± 6.05	20.16 ± 2.84	15.55 ± 2.79
$t\bar{t}$	101.34 ± 11.94	83.65 ± 11.53	20.07 ± 4.56	5.12 ± 1.70	2.31 ± 1.48
Single top	16.28 ± 5.19	17.26 ± 5.22	5.42 ± 3.23	2.00 ± 1.77	$1.68^{+2.02}_{-1.68}$
W+jets	27.77 ± 4.02	37.05 ± 4.34	14.24 ± 2.44	6.11 ± 0.97	5.87 ± 1.08
Z+jets	2.02 ± 0.91	1.10 ± 0.68	0.33 ± 0.09	0.15 ± 0.04	0.15 ± 0.02
Diboson	7.20 ± 1.69	9.65 ± 2.00	4.59 ± 1.00	2.24 ± 0.47	2.59 ± 0.65
$t\bar{t}V$	12.28 ± 1.36	19.55 ± 3.51	8.71 ± 1.20	4.05 ± 0.72	2.53 ± 0.45
$t\bar{t}H$	0.56 ± 0.06	0.60 ± 0.06	0.17 ± 0.02	0.06 ± 0.02	0.03 ± 0.00
tWZ	1.66 ± 0.21	2.42 ± 0.46	1.17 ± 0.15	0.42 ± 0.09	0.39 ± 0.09

Table 2.9: Results of the background-only fit in the signal region for the single lepton channel of the search targeting the 2HDM+a tW+$E_{\mathrm{T}}^{\mathrm{miss}}$ signature. This fit includes only the control regions used to normalise the $t\bar{t}$ and W+jets backgrounds.

1ℓ analysis	
$\mu(t\bar{t})$	0.96 ± 0.08
μ(W)	1.01 ± 0.05
$1\ell + 2\ell$ combination	
$\mu(t\bar{t}\ 1\ell)$	0.96 ± 0.08
$\mu(t\bar{t}\ 2\ell)$	1.00 ± 0.03
μ(W)	1.01 ± 0.05
μ(WZ)	0.75 ± 0.26
$\mu(t\bar{t}Z)$	0.81 ± 0.16

Table 2.10: Background normalisation factors the tW+$E_{\mathrm{T}}^{\mathrm{miss}}$ analysis

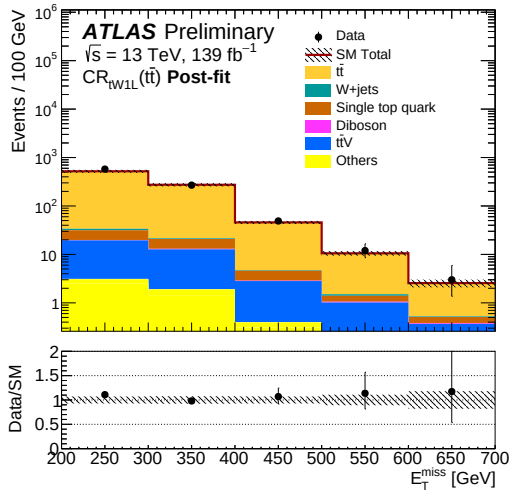

(a) $E_{\mathrm{T}}^{\mathrm{miss}}$ distribution in CR($t\bar{t}$)

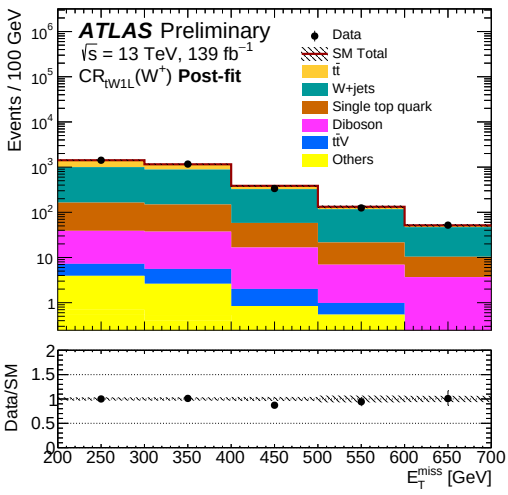

(b) $E_{\mathrm{T}}^{\mathrm{miss}}$ distribution in CR(W^+)

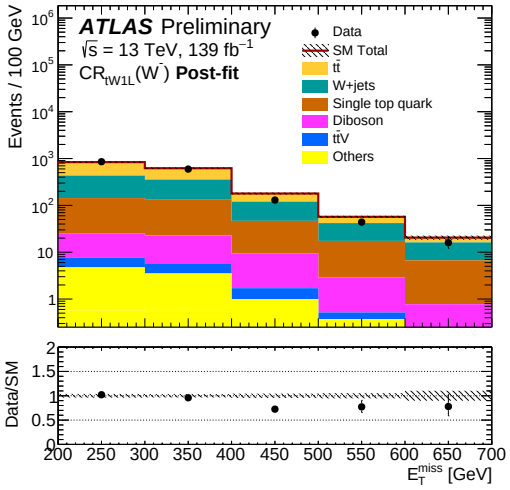

(c) $E_{\mathrm{T}}^{\mathrm{miss}}$ distribution in CR(W^-)

Figure 2.5: Post-fit distributions of the $E_{\mathrm{T}}^{\mathrm{miss}}$ variable in all CRs. Excellent data/MC agreement is observed. The uncertainty band on the ratio contains the MC statistical, experimental and modelling uncertainties.

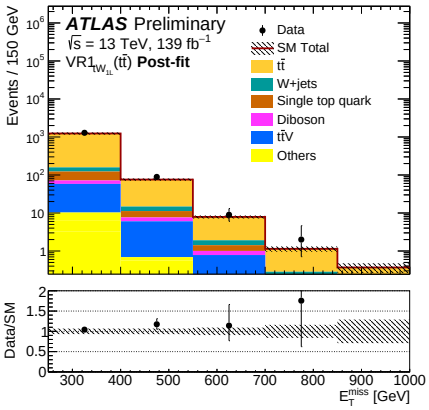

(a) $E_{\mathrm{T}}^{\mathrm{miss}}$ distribution in VR1($t\bar{t}$)

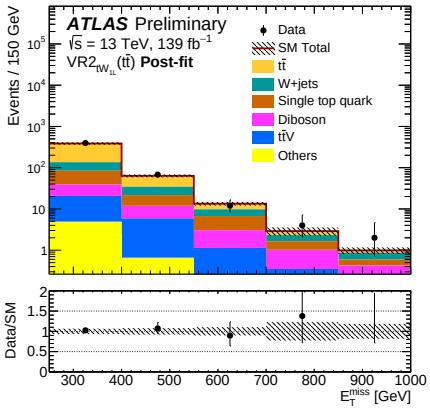

(b) $E_{\mathrm{T}}^{\mathrm{miss}}$ distribution in VR2($t\bar{t}$)

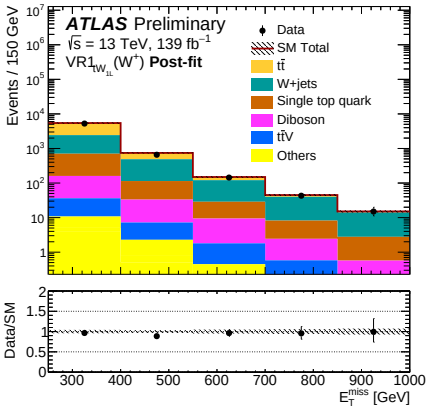

(c) $E_{\mathrm{T}}^{\mathrm{miss}}$ distribution in VR1(W^+)

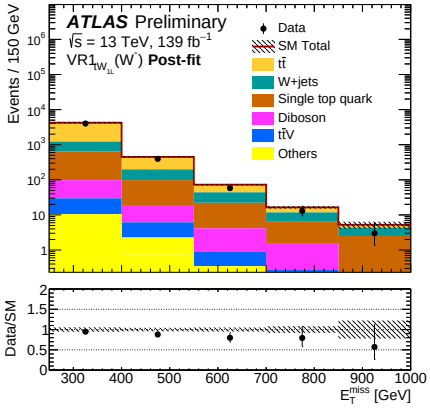

(d) $E_{\mathrm{T}}^{\mathrm{miss}}$ distribution in VR1(W^-)

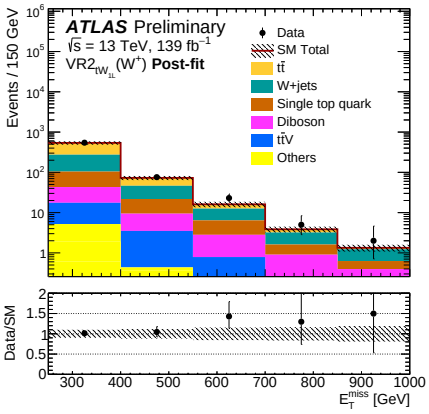

(e) $E_{\mathrm{T}}^{\mathrm{miss}}$ distribution in VR2(W^+)

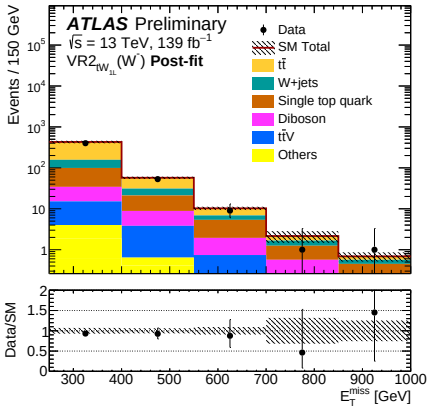

(f) $E_{\mathrm{T}}^{\mathrm{miss}}$ distribution in VR2(W^-)

Figure 2.6: Plots showing the $E_{\mathrm{T}}^{\mathrm{miss}}$ distribution in all VRs. Good agreement between data and MC in all regions is observed. The uncertainy band on the ratio includes MC statistical, experimental and modelling uncertainties.

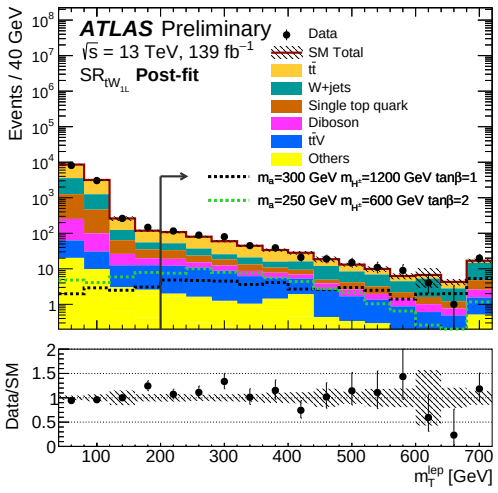

(a) m_{T}

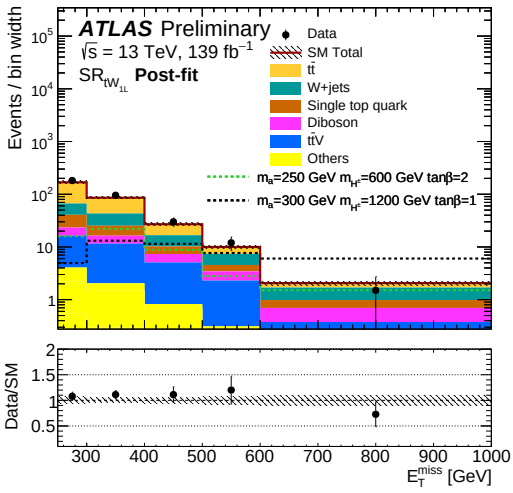

(b) $E_{\mathrm{T}}^{\mathrm{miss}}$

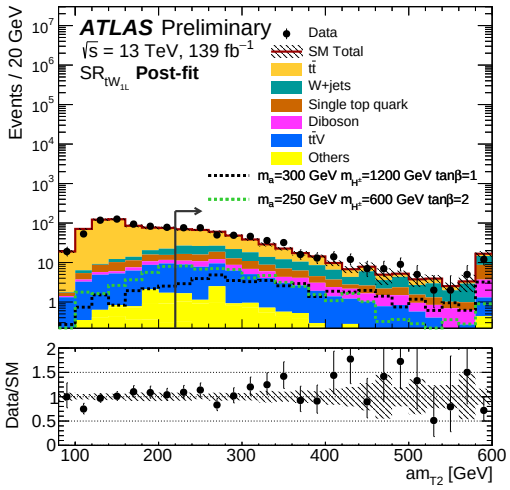

(c) am_{T2}

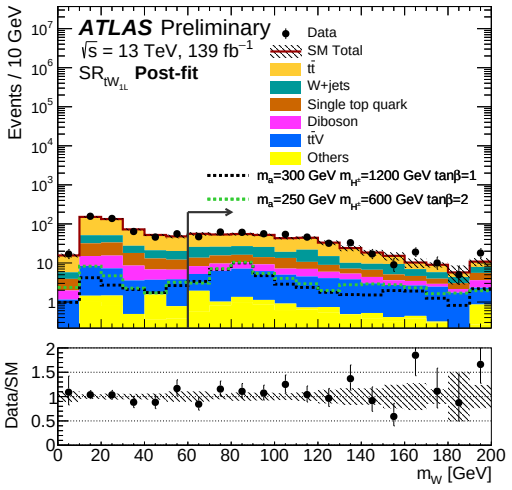

(d) $m_{\mathrm{W}}^{\mathrm{had}}$

Figure 2.7: Plots showing the post-fit N-1 distributions of the key kinematic variables. In these plots, all selections are applied except those on the variable being plotted. All uncertainties are included in the error band on the ratio. No significant excess is observed in the SR bins.

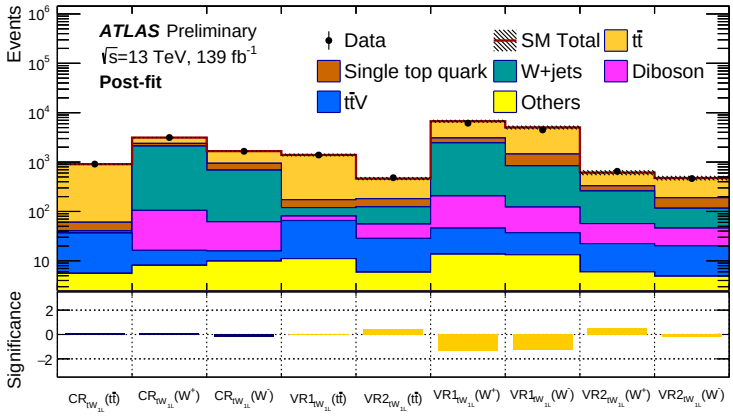

Figure 2.8: Summary plot showing the data/MC agreement in all control and validation regions for the single lepton channel of the search targeting the 2HDM+a tW+$E_{\mathrm{T}}^{\mathrm{miss}}$ signature. The uncertainty used to calculate the significance of the data/MC difference includes the statistical component on the MC and the data, as well as the total systematic uncertainty on the background estimate.

Model-dependent limits

In the absence of a significant excess, limits are set on the 2HDM+a model at 95% confidence limits using the previously described prescription. Model-dependent limits are set on the DMt and the DM$t + t\bar{t}$ signatures, in both the $m_a - m_{H\pm}$ and $m_{H\pm} - \tan\beta$ planes. For the DMt signature, $H^{\pm}$ masses are excluded upto 1250 GeV for $m_a = 100$ GeV, while for the DM$t + t\bar{t}$ signature masses above 1400 GeV are excluded. The observed limit of the statistical combination of the 1ℓ and 2ℓ channels is not as sensitive as the dedicated 1ℓ channel due to the 2σ excess in the 2ℓ SR.

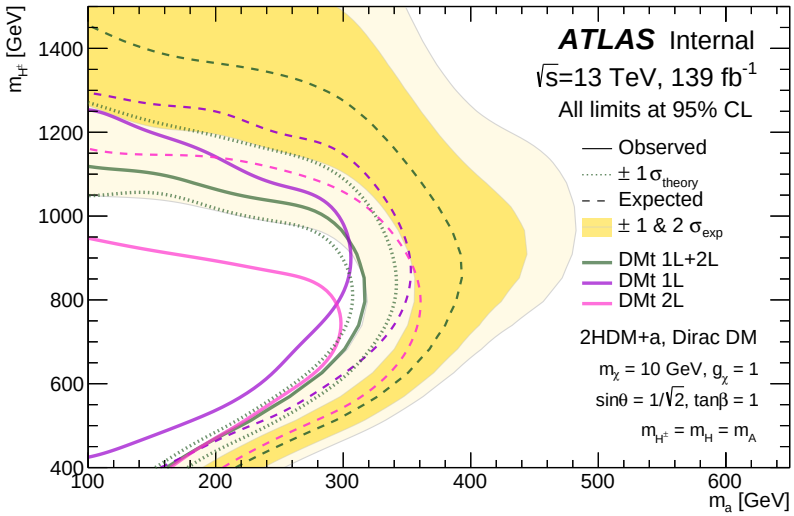

(a)

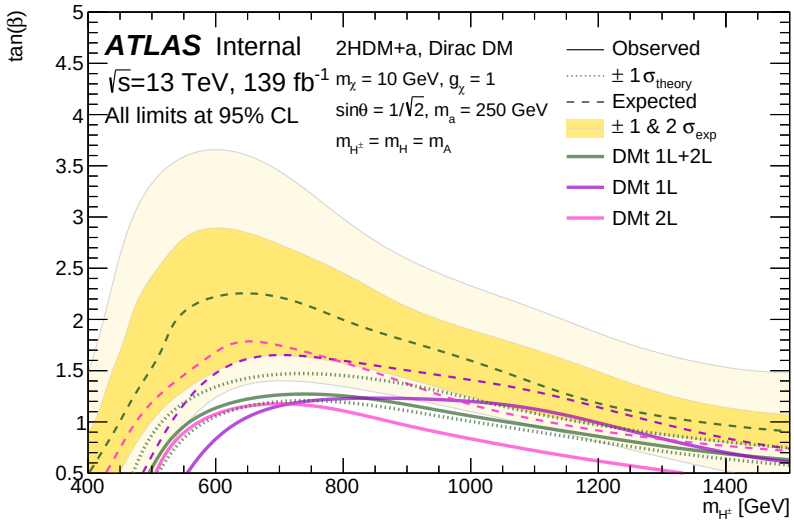

(b)

Figure 2.9: Plots showing the sensivitity to the 2HDM+a signal with the tW+$E_{\mathrm{T}}^{\mathrm{miss}}$ signature. Limits are shown in both the m_a-$m_{H^{\pm}}$ plane (a) and the $m_{H^{\pm}}$-tan(β) plane (b). Limits are shown for the analyses targeting the single lepton and di-lepton final states, along with the statistical combination of both channels.

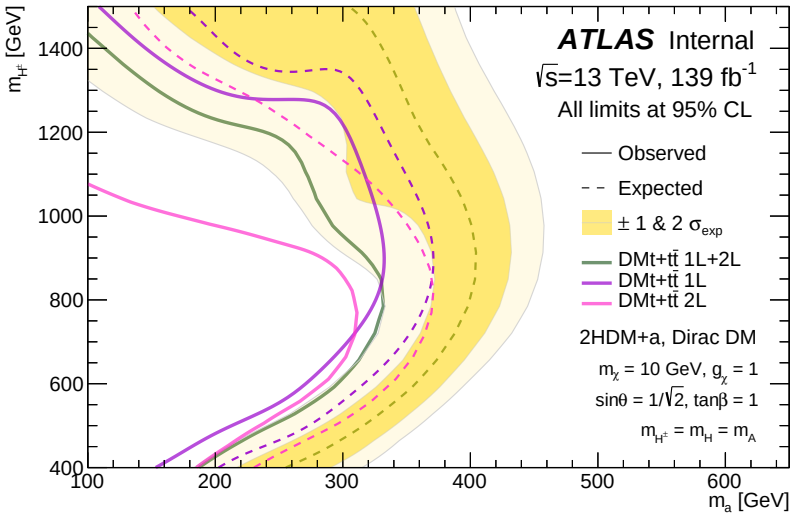

(a)

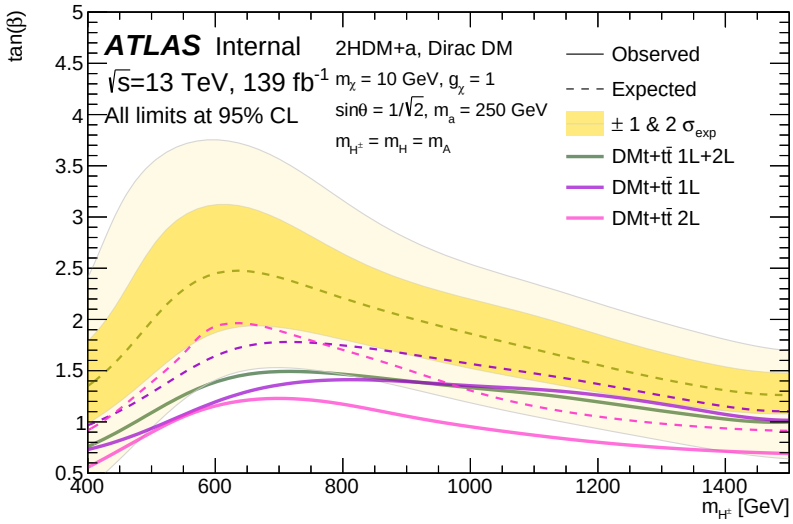

(b)

Figure 2.10: Plots showing the sensivitity to the 2HDM+a signal for both tW and $t\bar{t}$ signatures. Limits are shown in both the m_a-$m_{H^\pm}$ plane (a) and the $m_{H^\pm}$-tan(β) plane (b). Limits are shown for the analyses targeting the single lepton and di-lepton final states, along with the statistical combination of both channels.

Model-independent limits

In addition to model-dependent limits being set on the 2HDM+a signal model, with both tW and $tW + t\bar{t}$ signatures, 95% CL limits are set on any generic BSM processes using the model-independent fit strategy described in Section **??**. The limits are presented as limits on the *visible* cross-section, $\sigma_{\text{vis}} = \epsilon \cdot A \cdot \sigma_{BSM}$, where ϵ is the signal selection efficiency, A is the detector acceptance, and σ_{vis} is the production cross-section for a generic BSM process. To set limits on a generic BSM process, the SR definition from Table 2.3 are modified, such that the individual SR bins have no upper $E_{\text{T}}^{\text{miss}}$ limit and rather only a lower $E_{\text{T}}^{\text{miss}}$ threshold. The yields in these modified, 'inclusive' SR bins are shown in Table 2.11. The results of the model-independent fit are shown in Table 2.12, as 95% CL limits on the expected and observed number of signal events.

Inclusive signal regions					
$E_{\text{T}}^{\text{miss}}$ threshold [GeV]	> 250	> 300	> 400	> 500	> 600
Observed events	469	287	96	36	12
Fitted bkg events	431.47 ± 27.12	261.90 ± 20.10	90.65 ± 10.07	35.94 ± 5.22	15.54 ± 2.77
$t\bar{t}$	212.61 ± 25.01	111.14 ± 17.69	27.51 ± 7.36	7.44 ± 2.94	2.31 ± 1.48
Single top	43.28 ± 14.49	26.66 ± 11.76	9.35 ± 6.53	3.92 ± 3.85	$1.68^{+2.02}_{-1.68}$
W+jets	91.05 ± 7.64	63.29 ± 5.47	26.24 ± 2.82	11.99 ± 1.67	5.87 ± 1.08
Z+jets	3.76 ± 1.03	1.72 ± 0.69	0.62 ± 0.12	0.30 ± 0.05	0.15 ± 0.02
Diboson	26.26 ± 5.49	19.06 ± 3.92	9.42 ± 1.97	4.83 ± 1.01	2.59 ± 0.65
$t\bar{t}V$	47.01 ± 2.76	34.75 ± 2.39	15.27 ± 1.17	6.57 ± 0.48	2.53 ± 0.33
$t\bar{t}H$	1.42 ± 0.09	0.87 ± 0.07	0.26 ± 0.02	0.09 ± 0.02	0.03 ± 0.00
tWZ	6.07 ± 0.37	4.40 ± 0.31	1.99 ± 0.13	0.81 ± 0.08	0.39 ± 0.04

Table 2.11: Table showing the expected and observed yields in the modified signal regions for the determination of the model-independent limits.

Region	$\langle\epsilon\sigma\rangle_{\text{obs}}^{95}$[fb]	S_{obs}^{95}	S_{exp}^{95}
$\text{SR}_{1\text{L}}$ ($E_{\text{T}}^{\text{miss}} > 250$ GeV)	0.72	100.6	$66.7^{+32.7}_{-16.4}$
$\text{SR}_{1\text{L}}$ ($E_{\text{T}}^{\text{miss}} > 300$ GeV)	0.51	70.8	$54.1^{+16.0}_{-15.9}$
$\text{SR}_{1\text{L}}$ ($E_{\text{T}}^{\text{miss}} > 400$ GeV)	0.24	32.9	$29.4^{+10.1}_{-6.4}$
$\text{SR}_{1\text{L}}$ ($E_{\text{T}}^{\text{miss}} > 500$ GeV)	0.14	18.9	$18.7^{+7.6}_{-4.9}$
$\text{SR}_{1\text{L}}$ ($E_{\text{T}}^{\text{miss}} > 600$ GeV)	0.08	10.6	$12.0^{+2.7}_{-3.6}$

Table 2.12: Table showing the model-independent limits derived for the five modified inclusive SRs. Upper limits on the visible cross-sections of BSM physics between 0.08-0.72fb are excluded at 95% confidence limits, translating to an upper limit of around 100 events with a dataset of 139fb^{-1}.

Part II

High-Luminosity LHC studies

Chapter 3

Testbeam studies of FE-I4 and RD53A performance at HL-LHC

The Run-2 period of data taking concluded in 2018, with ATLAS having recorded a dataset totalling 139 fb^{-1}, making way for the start of Long Shutdown 2 (LS2). With LS2 comes the start of preparations for the next phase of the scientific programme of the LHC and ATLAS, the High-Luminosity phase. The High-Luminosity LHC (HL-LHC) will begin running in the mid-2020s, bringing instantaneous luminosities around 5 times higher than in Run-2, reaching $7.5 \times 10^{34}\,\text{cm}^{-2}\text{s}^{-1}$ at $\sqrt{s} = 14$ TeV. The total integrated luminosity to be recorded by ATLAS during this period is expected to total 3000-4000 fb^{-1}. Both the LHC and ATLAS will undergo numerous upgrades to prepare for the HL-LHC operations phase.

The first set of upgrades to the ATLAS detector, known as the Phase I upgrades, will take place in Long Shutdown 2 (LS2), between 2019-2021. The New Small Wheel (NSW) [16] will replace the current muon end-cap system, providing precision tracking and triggering capabilities. In addition, upgrades will be made to the electronics of the LAr calorimeter system, providing higher-granularity information to the L1 trigger [17].

Following the completion of Run-3 of LHC operations, both ATLAS and LHC will go into Long Shutdown 3 (LS3). During the High-Luminosity LHC (HL-LHC) phase, the instantaneous luminosity is estimated to result in an average of 200 inelastic *pp* collisions in each bunch-crossing, with bunch-crossings occuring every 25 ns. This instantaneous luminosity far exceeds the design of the ATLAS detector described in Chapter **??**. The increase in luminosity will render the current ID of the ATLAS detector inoperable, and hence a new tracker will be installed, known as the ATLAS Inner Tracker (ITk). The ITk will be constructed using only silicon pixel and strip modules, as these technologies are suited for high-occupancy, high-radiation environments. This Chapter documents studies performed on the performance of pixel modules for the upcoming ATLAS Inner Tracker

(ITk) upgrade. In particular, test beam studies were performed using FE-I4 modules, the pixel modules currently being used in the IBL, to validate the reconstruction and analysis workflow. Preliminary plots from the RD53a modules, a prototype version of the modules to be used in the ITk, are also shown.

3.1 ATLAS ITk upgrade

The ATLAS ITk, which is to be installed during the Phase II upgrades to the ATLAS detector, will replace the ATLAS ID during LS3. The ITk is an all silicon tracking detector, consisting of pixel and strip modules [18, 19]. Figure 3.1 shows the ATLAS ITk layout, where the blue elements correspond to the strip detector modules, while the red elements correspond to the pixel detector modules.

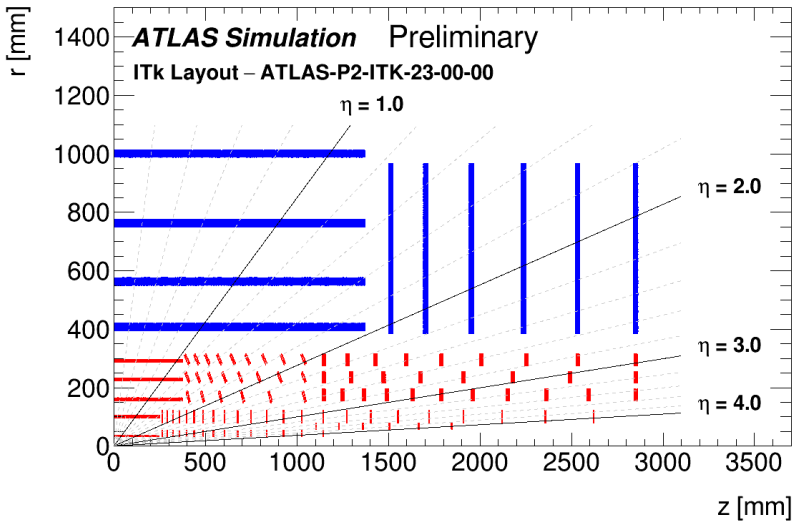

Figure 3.1: A schematic diagram, showing the ATLAS ITk layout for active detector elements. The detector elements shown in blue correspond to the strip detector, while the red elements correspond to the pixel detector.

The ITk aims to provide excellent tracking performance and efficiency, while operating in conditions where $\langle\mu\rangle = 200$, and also extending the tracking coverage upto $|\eta| < 4$. In addition to the challenging pileup conditions, the fluence is expected to be as high as $3 \times 10^{16}\, n_{\text{eq}}/\text{cm}^2$, and hence the ITk must be extremely radiation-hard.

The pixel detector forms the innermost 5 layers and is surrounded by the strip detector. Between the two subdetectors, as many as 13 hits will be recorded for charged particles traversing the detector. The increase in the tracking granularity in the ITk is expected to improve the current track efficiency performance, despite the harsh pileup conditions, while the rate of fake tracks being reconstructed is expected to reduce significantly. Figure

3.2 shows the track reconstruction efficiency and fake rate as a function of $|\eta|$ for simulated $t\bar{t}$ events, comparing the ITk performance with $\langle\mu\rangle = 200$ to the Run-2 performance.

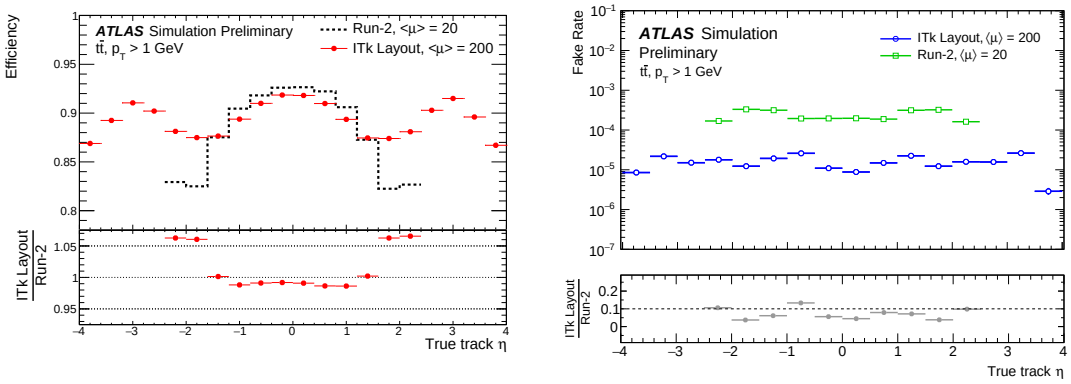

(a) (b)

Figure 3.2: Plots showing the track reconstruction efficiency (3.2a) and fake rate (3.2b) for simulated $t\bar{t}$ events, comparing the ITk performance with $\langle\mu\rangle = 200$ to the Run-2 performance [20].

3.2 Experimental setup

DESY beam

DESY, the Deutsches Elektronen-Synchrotron, provides test beam facilities to experimental teams, allowing tests of the performance of detector devices. The DESY-II synchrotron [21], which begin operations in 1987, accelerates electrons or positrons, with momenta selectable between 1-6 GeV. A diagram showing the layout of the DESY-II test beam facility is shown in Figure 3.3.

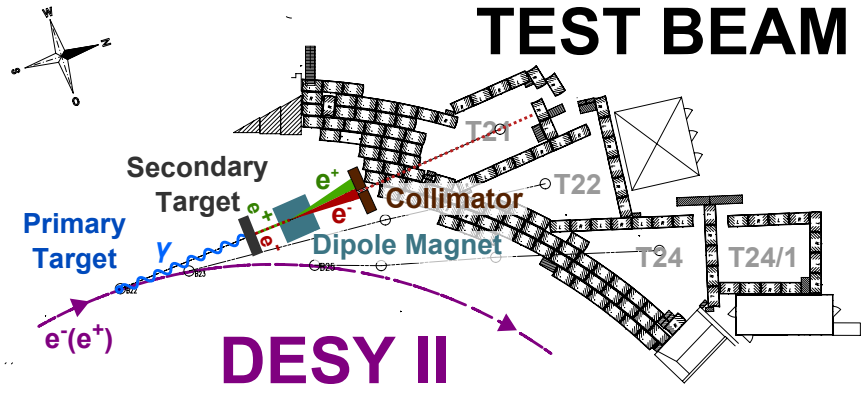

Figure 3.3: Diagram of the DESY-II test beam facility [21].

The primary target, a 7 μm thick fiber, is placed in the beam orbit, which creates bremsstrahlung photons. The bremsstrahlung photons exit the DESY-II beam, travelling

around 22m to hit the secondary targets. When these photons interact with the secondary target, electron-positron pairs are produced. The secondary targets are situated in front of the test beam facility dipole magnet, which allow the secondary electrons and positrons to be directed to three test beam halls, T21, T22 and T24.

EUDET setup

Test beam analyses at the DESY facility are performed using an EUDET-type beam telescope [22]. The telescope itself is a small tracking detector, comprising six silicon pixel sensors which are used to provide reference track hits, a triggering system which consists of four scintillators (two at the front of the telescope and two at the back) with photo multiplier tubes (PMTs) and a trigger logic unit (TLU), and finally a data acquisition (DAQ) system which reads out the hits and trigger information. A photograph of the EUDET telescope from a test beam in December 2018 is shown in Figure 3.4 for reference.

Figure 3.4: A photograph of the EUDET telescope at DESY from a test beam in December 2018. Here, the six telescope planes are clearly visible, with two RD53a modules situated between the two groups of three telescope planes.

The six telescope sensor planes are arranged into two sets of three sensors with space between to insert a device-under-test (DUT). Telescope track hits are provided by these six planes, each of which has a MIMOSA 26 CMOS sensor. Each MIMOSA 26 sensor has 1152 columns and 576 rows of pixels, each of which is 18.4μm $\times$ 18.4μm. The total instrumented area of each telescope which can collect hit information, known as the active area, is 10.6 mm $\times$ 21.1 mm. A schematic diagram of the layout of the telescope planes is

given in Figure 3.5.

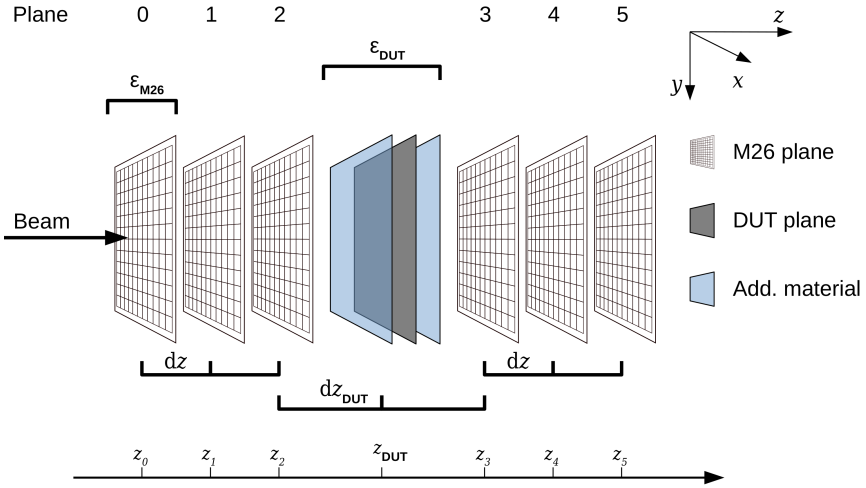

Figure 3.5: Schematic diagram of the layout of the six MIMOSA 26 telescope planes [22].

The telescope planes operate at a 80 MHz clock rate, with each row taking 16 cycles to be read out. This translates to the telescope being able to be fully read out approximately 8680 times per second. Reading out at this rate would produce huge amounts of data, much of which would be of no use to the subsequent analysis, and hence a trigger system is employed to only read out the telescope planes and DUTs when there is a signal, i.e. a particle passes through the telescope. When a particle enters the scintillator material, ionisation can occur which leads to the subsequent emission of photons. If all four PMTs detector photons being emitted by their respective scintillators, the trigger is passed and the telescope and DUTs are read out.

3.3 Reconstruction and analysis

Reconstruction of test beam data is performed using the EUTelescope framework using a multi-step approach. The most important steps are *clustering*, *hit making*, *alignment* and finally *track-fitting*. A schematic diagram of the EUTelescope reconstruction steps is shown in Figure 3.6.

In order to measure the efficiency of a DUT, the reconstructed tracks from the telescope planes must be matched to hits in the DUT. The global efficiency of a DUT is given by

$$\epsilon_{\mathrm{DUT}} = \frac{N_{\mathrm{tracks,\ matched}}}{N_{\mathrm{tracks}}} \,, \tag{3.3.1}$$

where N_{tracks} is the total number of telescope tracks and $N_{\mathrm{tracks,\ matched}}$ is the subset of those which have a matching hit in the DUT. After HL-LHC radiation doses, the desired efficiency of each pixel module is to be above 97%. The in-pixel efficiency measures the efficiency of each pixel, and is calculated by taking the ratio of the

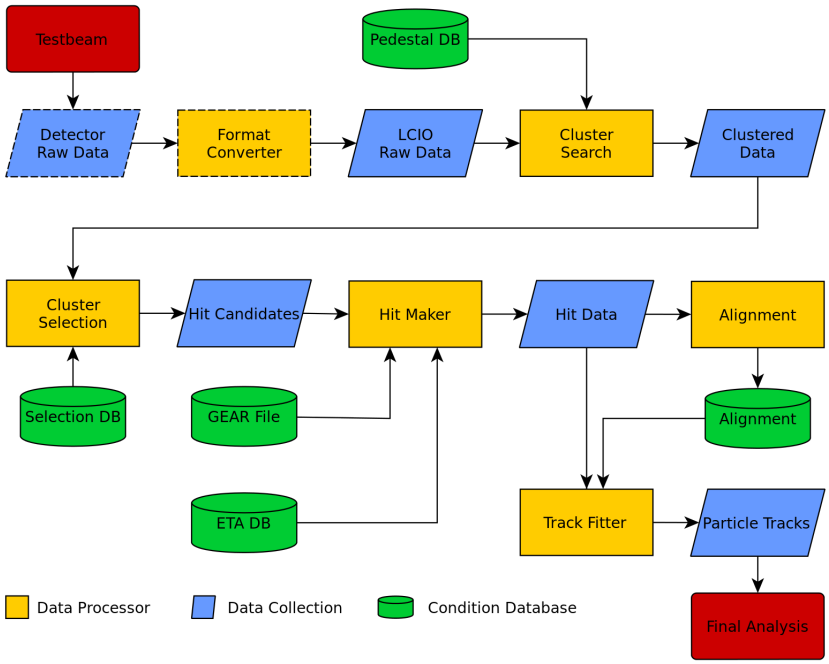

Figure 3.6: Diagram showing the workflow for reconstructing data taken at test beams, using the EUTelescope framework.

Two FE-I4 modules [23] were used to validate the reconstruction and analysis setup. These modules have 26880 pixels arranged in 80 columns and 336 rows, with an asymmetric pixel pitch of 250 μm by 50 μm. Hitmaps for the two FE-I4 modules are shown in Figure 3.7.

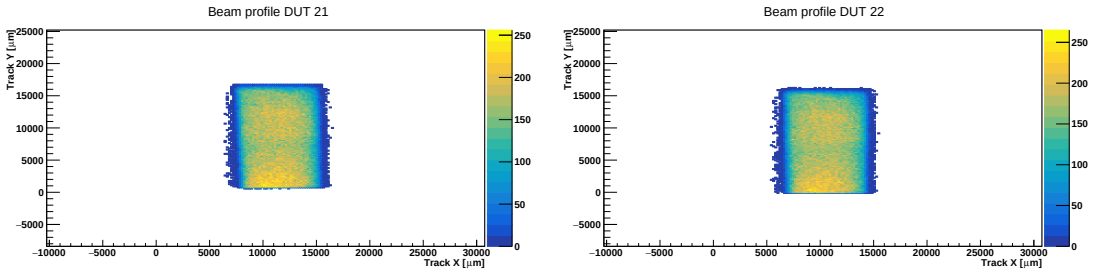

(a) (b)

Figure 3.7: Hitmaps for the two FE-I4 DUTs. All hits recorded are in the shadow of the scintillators, as hits on the sensor outside the scintillator area would not trigger the read out.

One FE-I4 module was irradiated to fluences representative of that expected in the HL-LHC, such that the efficiency could be compared with the efficiency at the start of HL-LHC operations. The global efficiency of the unirradiated module, 'DUT 21', was found to be 97.5%, while for the irradiated module, 'DUT 22', the global efficiency was found to be 95.1%. In order to account for reconstruction inefficiencies, the relative efficiency of the

irradiated DUT to the unirradiated DUT is found by taking the ratio of their global efficiencies. The relative efficiency of the irradiated module is 97.5%. The global and in-pixel efficiency maps for these two modules are shown in Figure 3.8.

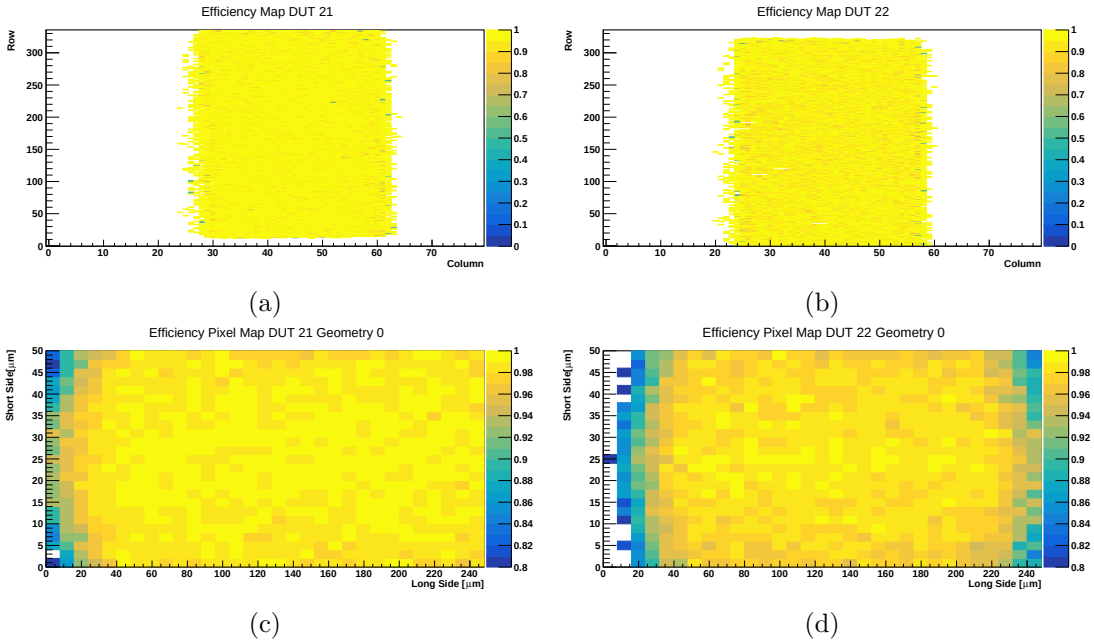

Figure 3.8: Plots showing the global (3.8a and 3.8b) and in-pixel efficiency maps (3.8c and 3.8d) for the two FE-I4 modules.

Initial studies on using the reconstruction framework described earlier were performed for the RD53A hybrid [24], which is a prototype version of the eventual ITk pixel modules. Work on the reconstruction and analysis of RD53A test beam data is on-going at the time of writing.

Chapter 4

Sensitivity to $\tilde{\chi}_1^{\pm}\tilde{\chi}_2^0$ pair-production at the HL-LHC

This chapter explores the potential sensivitivity of a search for chargino-neutralino pair-production using the ATLAS detector during the HL-LHC phase of operation. The HL-LHC is expected to begin operation in the latter half of the 2020's, bringing instantanenous luminosities around an order of magnitude higher than those currently at the LHC (7.5×10^{34}), along with an increase in centre-of-mass energy to $\sqrt{s} = 14$ TeV. It is expected that by the end of the HL-LHC phase, ATLAS will have taken 3000fb^{-1} of data, an expected ten-fold increase over the combination of Runs 2 and 3.

Along with the increased luminosity and collision energy delivered by the LHC, the ATLAS detector will be undergoing major upgrades in Long Shutdown 3 (LS3), providing an overhaul of many of the detector's subsystems. Of particular note is the new Inner Tracker (ITk), which will replace the current innermost tracking layers of the current ATLAS detector, vastly improving on the vertex resolution which will enable accurate track reconstruction in collisions with an average number of interactions per bunch-crossing, $\langle\mu\rangle$, of 200. Figure 4.1 shows a simulated $t\bar{t}$ event display from the ATLAS ITk in the expected pileup conditions at the HL-LHC.

With the increased centre-of-mass energy and the expected 3000fb^{-1} dataset, the physics analysis potential of the HL-LHC is unprecedented. Much of the HL-LHC physics program will be devoted to precision measurements of properties related to the Higgs boson and its relationship with the symmetry breaking mechanism of the electroweak sector of the SM. First sensitivity to the Higgs self-coupling is expected to be possible in the $HH \to b\bar{b}\gamma\gamma$ channel through both a conventional cut-and-count analysis [25] and a multivariate analysis [26]. This measurement will be used in combination with measurements in other final states, such as $b\bar{b}\tau\tau$ and $b\bar{b}b\bar{b}$ [27], further increasing sensitivity. It is also expected that measurements of the largest Higgs boson couplings to SM particles will be done with percent-level precision. Along with increased precision in measurements and

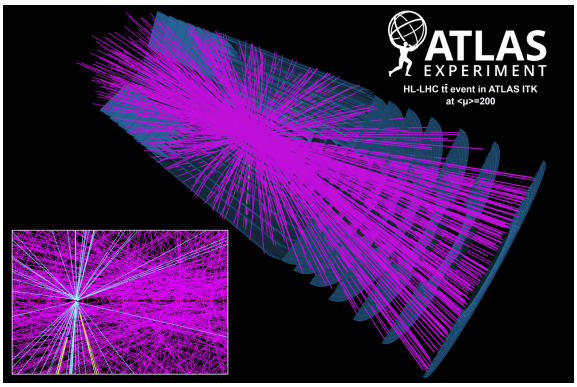

Figure 4.1: An event display of a simulated $t\bar{t}$ event in the ATLAS ITk at the HL-LHC, where there are an expected 200 interactions per bunch-crossing.

sensitivity to SM properties, the HL-LHC will also bring increased sensitivity to TeV-scale new physics. This chapter describes one such prospects analysis, forming part of a plethora of sensitivity studies [28].

The analysis described in this chapter targets the same signal model as in Chapter **??**, with a final state of a single electron/muon, two b-jets and $E_{\mathrm{T}}^{\mathrm{miss}}$. The sensitivity is assessed in the context of current expected HL-LHC conditions. Due to the huge dataset expected to be collected at the HL-LHC, the sensitivity is expected to reach far beyond the Run-2 sensitivity, and as such, mass upto 1500 GeV are considered for the $\tilde{\chi}_1^{\pm}/\tilde{\chi}_2^0$.

4.1 MC simulation

Signal samples for this study are generated at leading-order in QCD, with upto two additional partons, using MadGraph5_aMC@NLO [29] for the matrix element (ME), while Pythia 8 [30] is used for the parton showering (PS), hadronisation and underlying event (UE). The A14 tune is used for Pythia 8 [31] while the NNPDF23LO PDF set [32] is used for generation. Partons are matched between the ME and PS using the CKKW-L [33] prescription, with the scale used for matching set to one quarter of the mass of the $\tilde{\chi}_1^{\pm}/\tilde{\chi}_2^0$. The cross-sections are evaluated at next-to-leading order in α_s and next-to-leading logarithmic precision for the resummation of soft gluon emissions. The nominal cross section is determined by evaluating the cross section predictions with different PDF sets, factorisation and renormalisation scales [34]. Similarly to the analyses previously described, numerous generator configurations were used to generate the MC background samples. These are summarised in Table 4.1.

All samples are generated at truth-level. A parameterised simulation of the detector response is applied to all truth-level MC samples. This will be described in more detail in the following section.

Process	Generator + fragmentation/hadronisation	Tune	PDF set	Cross-section order
W/Z+jets	Sherpa 2.2.1 [?]	Default	NNPDF30NNLO [?]	NNLO
$t\bar{t}$	Powheg-Box v2 + Pythia 8.186	A14	NNPDF23LO [?]	NNLO+NNLL
Single top	Powheg-Box v1 or v2 + Pythia 6.428 [?]	Perugia2012 [?]	CT10 [?]	NNLO+NNLL
Diboson (fully leptonic)	Sherpa 2.2.1	Default	NNPDF30NNLO	NLO
(semi leptonic)	Powheg-Box v1 + Pythia 8.186	AZNLO [?]	CTEQ6L1	NLO
Higgs	Powheg-Box v2 + Pythia 8.186	AZNLO	CTEQ6L1	NNLO+NNLL

Table 4.1: Summary table showing the ME and PS configurations used to generate the SM MC samples for this study.

4.2 Detector simulation

In order to make meaningful predictions of sensitivity, a simulation of the ATLAS detector at the HL-LHC was developed through a set of parameterised smearing functions. These functions, known as the UpgradePerformanceFunctions, simulate the detector response by smearing the kinematic and angular properties of the physics objects, as well as providing additional collision vertices to simulate the pileup conditions at the HL-LHC. The treatment of each object relevant to this chapter will be discussed separately. Some shorthand will now be introduced for the following sections. $R(m,n)$ represents a random number drawn from a uniform distribution in the range m to n. $G(\mu,\sigma)$ represents a number drawn from a Gaussian distribution with a mean, μ, and a standard deviation, σ.

Leptons

The steps taken in the reconstruction of charged leptons is highly dependent on the generation of lepton being considered, but there are some common steps. Lepton ID working points are assigned for all three generations of charged leptons, and the detector response to the E_T for electrons and taus and p_T for muons is simulated. The charge-flip probability (the probability that the reconstructed lepton has the opposite charge to its true value), $P(\ell^{\pm}_{truth} \rightarrow \ell^{\mp}_{reco})$, is explicitly parameterised for electrons and is also possible for muons. Finally, the misreconstruction of an electron as a photon is parameterised.

A parameterisation of the lepton ID efficiencies is used in order to choose which lepton ID working points the lepton has passed. For each lepton generation there are three ID efficiency parameterisations, one corresponding to each working point. These parameterisations can be seen in Figure A.1. For a given lepton, the three ID efficiencies corresponding to the ID working points are retrieved, and all which satisfy $R(0,1) < \epsilon^i_{ID}$, with $i = 1,2,3$, are passed.

The p_T resolution for leptons is simulated differently for muons than for electrons and taus. For the former, the key quantity is the charge (in units of e) to transverse momentum ratio, $\frac{q}{p_T}$, while for electrons and taus it is the energy, E. For both quantities, the 'reconstructed' value is as follows:

$$\begin{aligned} E_{reco} &= E_{truth} + G(0, \Delta E) \\ \left(\frac{q}{p_T}\right)_{reco} &= \left(\frac{q}{p_T}\right)_{truth} + G\left(0, \Delta\left(\frac{q}{p_T}\right)\right) \end{aligned} \tag{4.2.1}$$

Here, ΔE and $\Delta\frac{q}{p_T}$ denote the resolutions on the respective quantity. The reconstructed muon transverse momentum is then given by $p_T^{reco} = \left|\left(\frac{q}{p_T}\right)^{-1}_{reco}\right|$, while for electrons and taus it is given by $p_T^{reco} = p_T^{truth} \times \frac{E_{reco}}{E_{truth}}$.

The charge-flip probability for electrons is parameterised in η and differs slightly for the three ID working points, as can be seen in Figure A.1. The charge-flip probability is determined by the tightest working point which is passed by the electron. A charge-flip occurs if the following condition is satisfied; $R(0,1) < P(e^{\pm}_{truth} \to e^{\mp}_{reco})$. For muons, particularly high-p_T or η muons, can undergo a charge flip when the $\frac{q}{p_T}$ is smeared.

Finally, electrons being misreconstructed as a photons is simulated through a parameterisation in η. For electrons with a $p_T > 20$ GeV, the probability of an electron being reconstructed as a photon is 2% for electrons with $|\eta\langle 1.37$ and is 5% for electrons with $|\eta\rangle 1.52$. An electron is misreconstructed as a photon if $R(0,1) < P(e \to \gamma)$.

Jets and flavour tagging

To simulate jet reconstruction, the first step of the detector simulation process is to smear the jet energy and p_T. The jet p_T is smeared by a multiplicative factor, $G\,(1, \Delta E)$, where ΔE represents the relative jet energy resolution determined from the parameterisation shown in Figure A.3a. The jet energy is smeared by multiplying the true jet energy by $\frac{p_T^{smeared}}{p_T^{truth}}$.

Jet flavour-tagging, in particular the tagging of jets originating from b-quarks, is of great importance to the study described in this chapter. The b-tagging working point used in this study has a b-tagging efficiency $\epsilon_b = 70\%$, which has much-improved light-jet rejection compared to the $\epsilon_b = 85\%$ working point. The flavour-tag efficiency, ϵ^b_{ftag}, is parameterised in jet p_T and η, and can be seen in Figure A.3b. Jets which have originated from a b-quark at truth-level are b-tagged if $R(0,1) < \epsilon^b_{ftag}$. The misreconstruction of jets as electrons, taus and photons is simulated by parameterising the so-called 'fake rate'. This is rate at

which an object is misreconstructed as another object.

$E_{\mathrm{T}}^{\mathbf{miss}}$

Smearing the $E_{\mathrm{T}}^{\mathrm{miss}}$ requires two steps. At truth-level, the missing transverse energy, $E_{T,truth}^{miss}$, is the sum of the transverse energies of all neutral particles in the event; in this study, only neutrinos and neutralinos contribute.

To account for mismeasurement due to pileup, $E_{T,truth}^{miss}$ is smeared by adding an additional term, $E_{T,pileup}^{miss}$, drawn randomly from the distribution shown in Figure A.4a. The $E_{\mathrm{T}}^{\mathrm{miss}}$ resolution, ΔE_T, is then determined from the parameterisation shown in Figure A.4b, using the sum of the neutral particle and pileup $E_{\mathrm{T}}^{\mathrm{miss}}$ components as an input. The final $E_{\mathrm{T}}^{\mathrm{miss}}$ is then give as:

$$E_T = E_{T,truth}^{miss} + G(0, \Delta E_T) \tag{4.2.2}$$

Kinematic distribution comparison

The effects of the detector simulation described in this section can be see in Figure 4.2. The 'truth-level' $t\bar{t}$ distribution includes no detector effects, the 'truth-level with smearing' $t\bar{t}$ distributions include the detector simulation described in this section, while the 'reco-level' sample is reconstructed using the full ATLAS detector simulation.

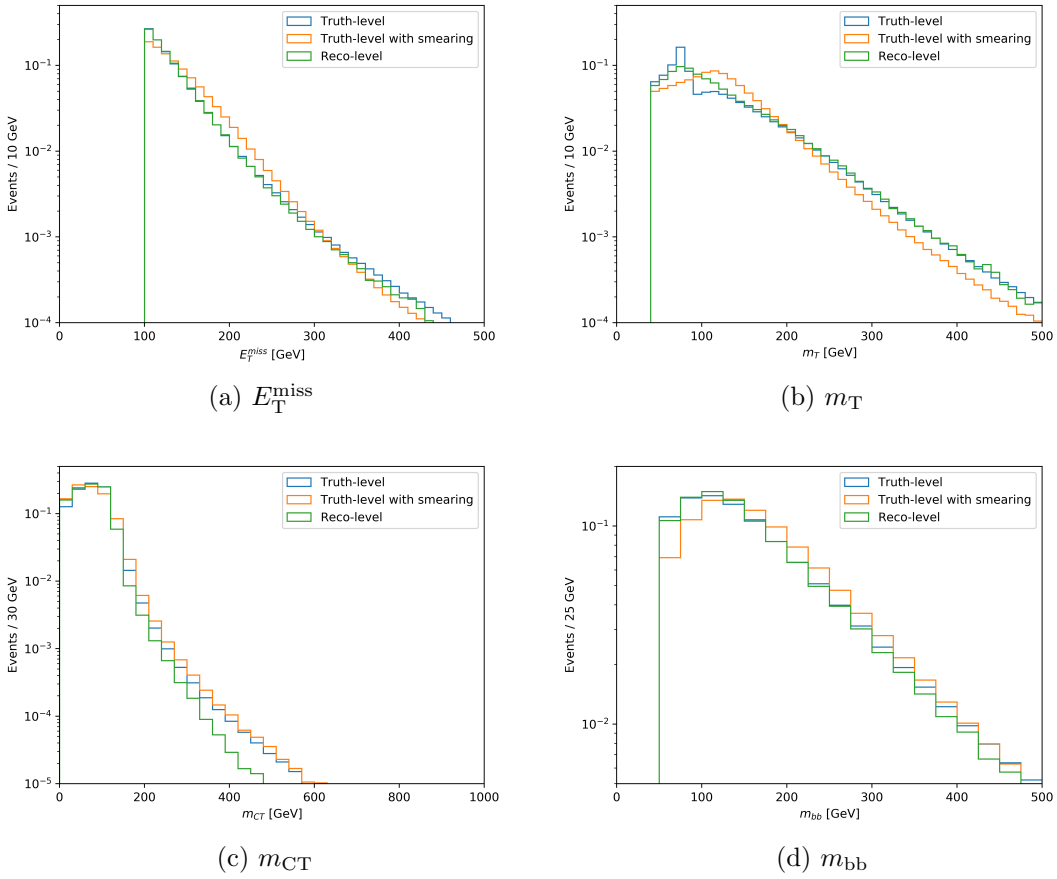

(a) $E_{\mathrm{T}}^{\mathrm{miss}}$ (b) m_{T}

(c) m_{CT} (d) m_{bb}

Figure 4.2: The E_T^{miss}, m_T, m_{CT} and m_{bb} distributions at truth-level, truth-level with the detector smearing described in this section, and a fully reconstructed samples. All distributions are normalised to unity to compare only the shape of the distributions and not normalisations.

4.3 Event selection

The object definitions used to reconstruct the leptons and jets are summarised in Table 4.2 and Table 4.3, respectively.

	Electrons	Muons
p_{T}	25 GeV	25 GeV
$\lvert\eta\rvert$	< 2.47	< 2.7
ID	Tight	Medium

Table 4.2: A summary of the object definitions for leptons in the HL-LHC projection.

Similarly to the 36.1fb^{-1} analysis described in Chapter 1, a number of preliminary selections are applied to select events with the single lepton, two b-jet topology, as shown in Table 4.4.

	jets	b-jets
p_{T}	25 GeV	25 GeV
$\lvert\eta\rvert$	< 2.5	< 2.5
Jet radius (R)	0.4	0.4
b-tagging WP	-	70%

Table 4.3: A summary of the object definitions for jets in the HL-LHC projection.

Preselection	
Leptons ($p_T \geq 25$ GeV)	$1e$ or 1μ
Jets ($p_T \geq 25$ GeV)	2 or 3
b-jets ($p_T \geq 25$ GeV)	2
m_{T}	≥ 40 GeV
m_{bb}	≥ 50 GeV
$E_{\mathrm{T}}^{\mathrm{miss}}$	≥ 200 GeV

Table 4.4: A summary of the preliminary selections used for for the HL-LHC projection.

The loose cuts on $m_{\mathrm{T}}$and $m_{\mathrm{bb}}$are employed to combat MC mismodelling seen in the analysis described in Chapter **??**, while the cut on $E_{\mathrm{T}}^{\mathrm{miss}}$ is used to both reduce the SM background and target events containing two $\tilde{\chi}_1^0$ in the final state.

Events passing the preliminary selections listed in Table 4.4 are used as inputs to Boosted Decision Tree (BDT) classifiers. The BDTs are implemented in Toolkit for Multivariate Data Analysis [35]. In this study, binary classification is performed such that the output of the BDT is a single value $\in [-1, 1]$. The key discriminatory variables which are given to the BDT classifiers as inputs are the $E_{\mathrm{T}}^{\mathrm{miss}}$, m_{T}, m_{CT}, m_{bb} and $\Delta R(\mathrm{b}_1, \mathrm{b}_2)$. Along with these, the transverse momentum of the lepton and the two b-jets are useful for background rejection. The distributions of $E_{\mathrm{T}}^{\mathrm{miss}}$, $m_{\mathrm{T}}$and $\Delta R(\mathrm{b}_1, \mathrm{b}_2)$for the signal are highly dependent upon the mass and the mass difference of the $\tilde{\chi}_1^{\pm}/\tilde{\chi}_2^0$and $\tilde{\chi}_1^0$, and as such having one classifier which performs equally well across the entire phase space is extremely difficult to achieve. To aid in this, three BDT classifiers are trained, targeting 'low', 'intermediate' and 'high' mass-splittings, ΔM = m($\tilde{\chi}_1^{\pm}/\tilde{\chi}_2^0$) - m($\tilde{\chi}_1^0$). SR-Low targets $\Delta M < 300$ GeV, SR-Med targets $\Delta M \in [300, 600]$ GeV and SR-High targets $\Delta M > 600$ GeV. The signal grid, highlighted with the three targeted regions, is shown in Figure 4.3.

Due to the limited number of MC events in each individual signal sample, all signal samples in each mass-splitting regime ('low', 'intermediate' or 'high' ΔM) are summed together with an equal weight of 1. The sum of signals for each mass-splitting region provide a high-statistics signal sample on which to train the BDTs, with kinematic distributions representing a 'pseudo-average' of the individual signal samples. A benchmark

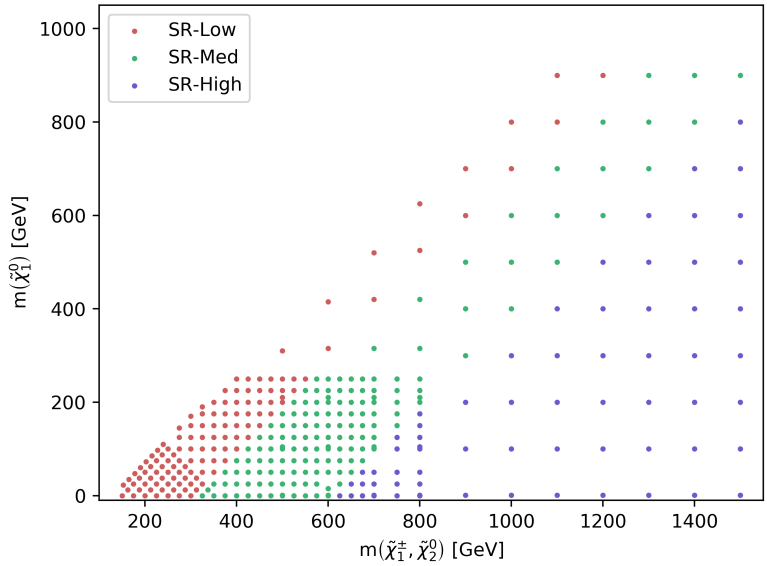

Figure 4.3: Plot showing the separation of the mass plane into the three defined categories.

signal is chosen from each mass-splitting region for the purposes of comparing the kinematic distributions of signal and background, and for later deriving an optimal cut on the BDT output. The kinematic distributions forming inputs to the BDTs are shown, with benchmark signals overlaid, in Figure 4.4.

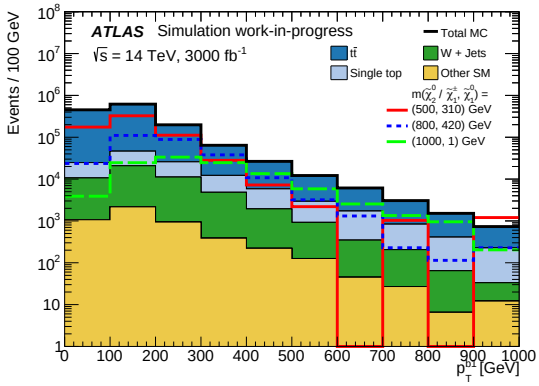

(a) p_T^{b1}

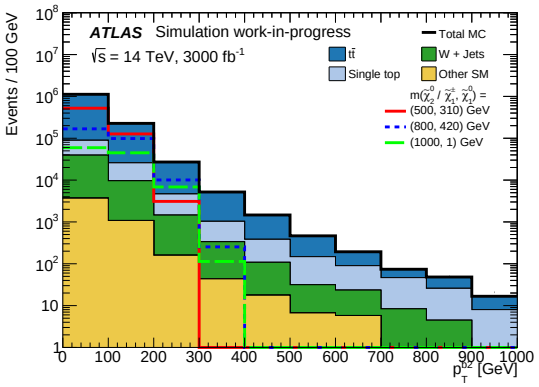

(b) p_T^{b2}

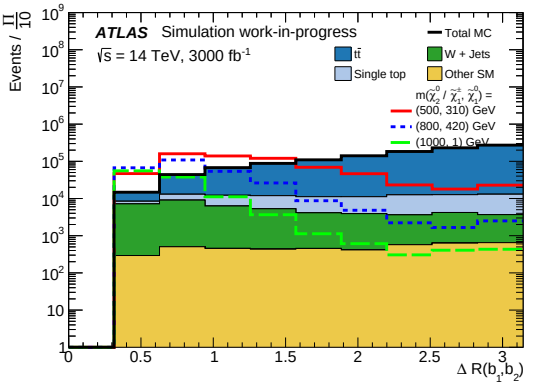

(c) $\Delta R(b1, b2)$

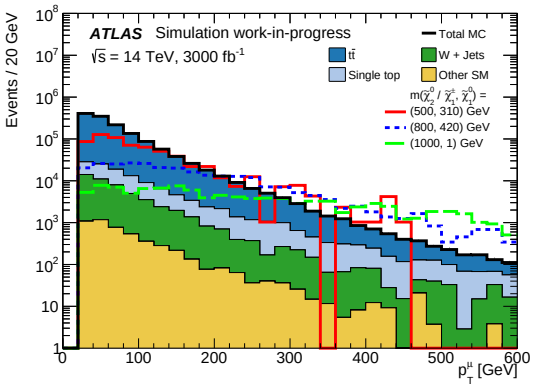

(d) $p_T^{\ell 1}$

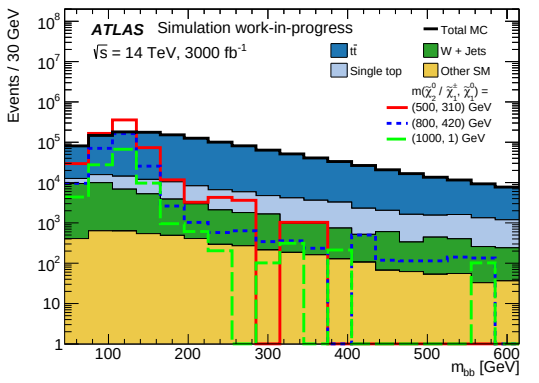

(e) m_{bb}

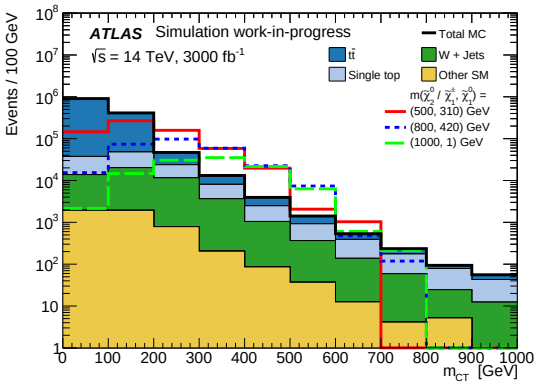

(f) m_{CT}

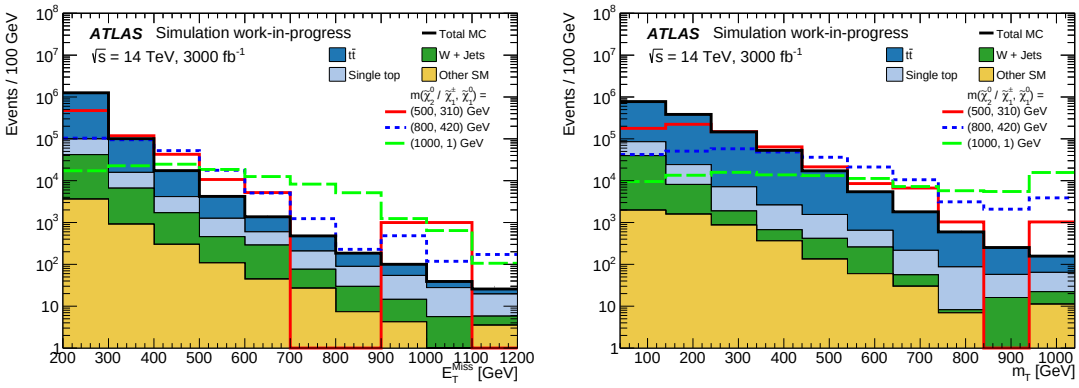

(g) $E_{\mathrm{T}}^{\mathrm{miss}}$ (h) m_{T}

Figure 4.4: Kinematic and angular distributions for the BDT input variables at the preselection-level.

The estimate for signal and background yields in the SRs is obtained by placing a cut on the output of the BDTs. The optimal cut value is derived by scanning over the BDT output with an increasing lower bound, and calculating the binomial significance, Z_n, for that region's benchmark model and the SM background. The optimal cuts are shown in Table 4.5.

SR	Signal benchmark $m(\tilde{\chi}_1^{\pm}/\tilde{\chi}_2^0, \tilde{\chi}_1^0)$ [GeV]	BDT range
SR-M1	(500, 310)	> 0.25
SR-M2	(800, 420)	> 0.35
SR-M3	(1000, 1)	> 0.30

Table 4.5: Benchmark signal models and the corresponding optimised BDT output cut, derived by maximising the binomial significance, Z_n of the benchmark signal over the SM background.

The BDT output distributions for the SM backgrounds and the benchmark signal point for each region is shown in Figure 4.5. The arrows in these plots show the cut placed on the BDT output.

4.4 Systematic uncertainties

A joint strategy between the ATLAS and CMS collaborations was adopted for estimating systematic uncertaines for HL-LHC projection studies. For analyses with an existing Run-2 analysis, a prescription for extrapolating the current systematic uncertainties to 3000 fb^{-1} , where theoretical modelling uncertainties are expected to be half their current value. The extrapolation method for experimental uncertainties depend upon the system-

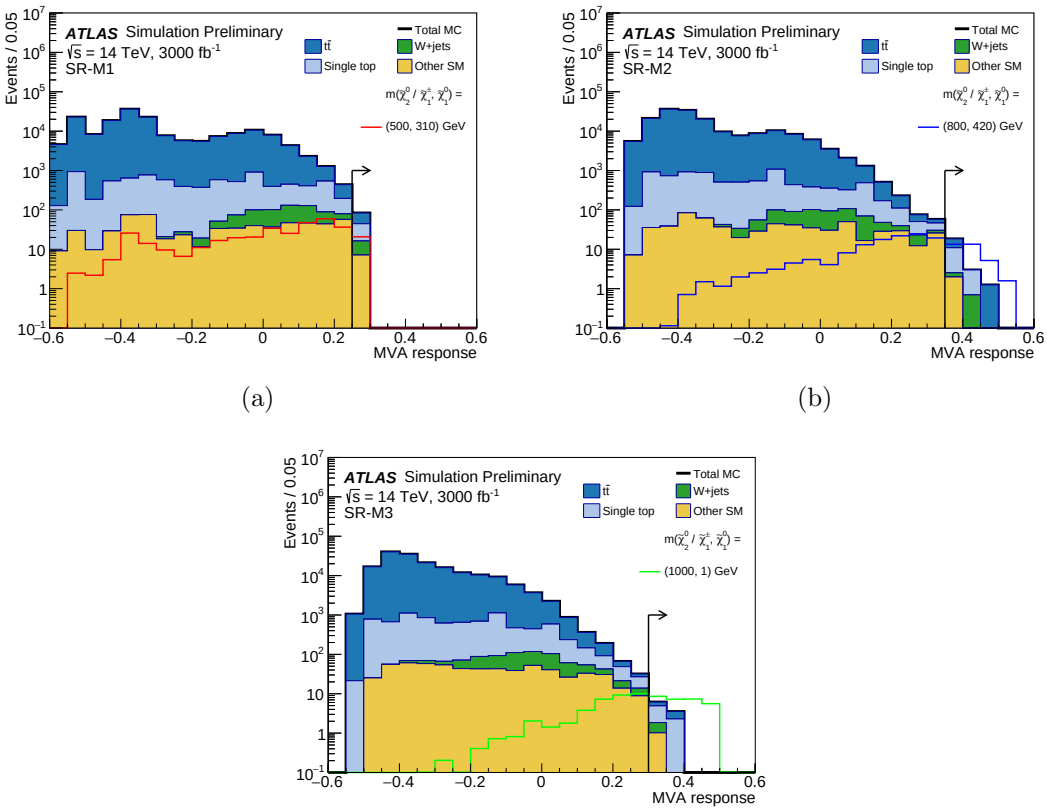

Figure 4.5: BDT outputs for HL-LHC projection. The arrow on each plot shows the cut placed on the BDT output, defining the SR.

atic under consideration and are provided as multiplicative factors which are applied to the Run-2 systematic uncertainties.

In this study, the systematics from the Run-2 analysis described in Chapter **??** are extrapolated from SR1Lbb-High, which is the signal region most kinematically similar to the regions presented in this analysis. The Run-4 extrapolated uncertainties are shown in Table 4.6.

SR1Lbb-High	
JET_JER_SINGLE_NP	10.30%
Wt-Interference	8.10%
ttbar-PS	6.40%
ttbar-Generator	5.50%
ttbar-Rad	5.00%
Wt-PS	4.50%
Wt-Rad	3.30%
JET_GroupedNP_2	2.90%
JET_GroupedNP_1	2.60%
MET_SoftTrk_Scale	2.00%
Wt-Generator	1.80%
EG_RESOLUTION_ALL	1.70%
JET_GroupedNP_3	1.10%
FT_EFF_B_systematics	0.98%
FT_EFF_C_systematics	0.97%
FT_EFF_Light_systematics	0.70%
MET_SoftTrk_ResoPara	0.45%
MET_SoftTrk_ResoPerp	0.42%
FT_EFF_extrapolation_from_charm	0.41%
EG_SCALE_ALL	0.36%
FT_EFF_extrapolation	0.18%
Pileup	0.17%
MUONS_ID	0.12%
JET_EtaIntercalibration_NonClosure	0.00%
EF_EFF	0.00%
MUONS_MS	0.00%
MUON_EFF_SYS	0.00%
Quadratic sum	18.13%

Table 4.6: A table showing the extrapolated systematic uncertainties based upon the Run-2 analysis.

.

4.5 Results

The yields after the BDT cuts shown in Table 4.5 are shown below in Table 4.7. Entries denoted by '-' indicate there were no events of that particular process in the corresponding region. Figure 4.6 shows the 95% CL exclusion limit for this channel, as well as the 5σ

Processes	SR-M1	SR-M2	SR-M3
$t\bar{t}$	38.9 ± 8.4	8.7 ± 3.3	2.5 ± 1.8
single top	28.3 ± 4.8	10.7 ± 3.2	5.4 ± 2.5
W+jets	22.2 ± 5.4	3.0 ± 2.0	2.0 ± 1.8
ttV	5.1 ± 2.4	2.0 ± 1.4	1.0 ± 1.0
Diboson	2.0 ± 2.0	-	-
total background	96.5 ± 11.8	24.4± 5.2	10.9 ± 3.4
$m(\tilde{\chi}_1^{\pm}/\tilde{\chi}_2^0, \tilde{\chi}_1^0) = (500, 300)$ GeV	20.7 ± 4.8	4.6 ± 2.3	1.0 ± 1.0
$m(\tilde{\chi}_1^{\pm}/\tilde{\chi}_2^0, \tilde{\chi}_1^0) = (800, 420)$ GeV	44.3 ± 2.3	33.6 ± 2.0	21.2 ± 1.6
$m(\tilde{\chi}_1^{\pm}/\tilde{\chi}_2^0, \tilde{\chi}_1^0) = (1000, 1)$ GeV	32.2 ± 1.8	31.9 ± 1.8	28.9 ± 1.7

Table 4.7: Expected signal and background yields. The errors are statistical uncertainties. Entries marked − indicate a negligible background contribution.

discovery potential. The three signal regions are combined by taking the best expected sensitivity for each signal point. The systematics band, represented by the yellow area around the 95% CL exclusion line includes the extrapolated experimental and modelling systematics on the SM backgrounds, as well as the statistical uncertainty on all MC samples.

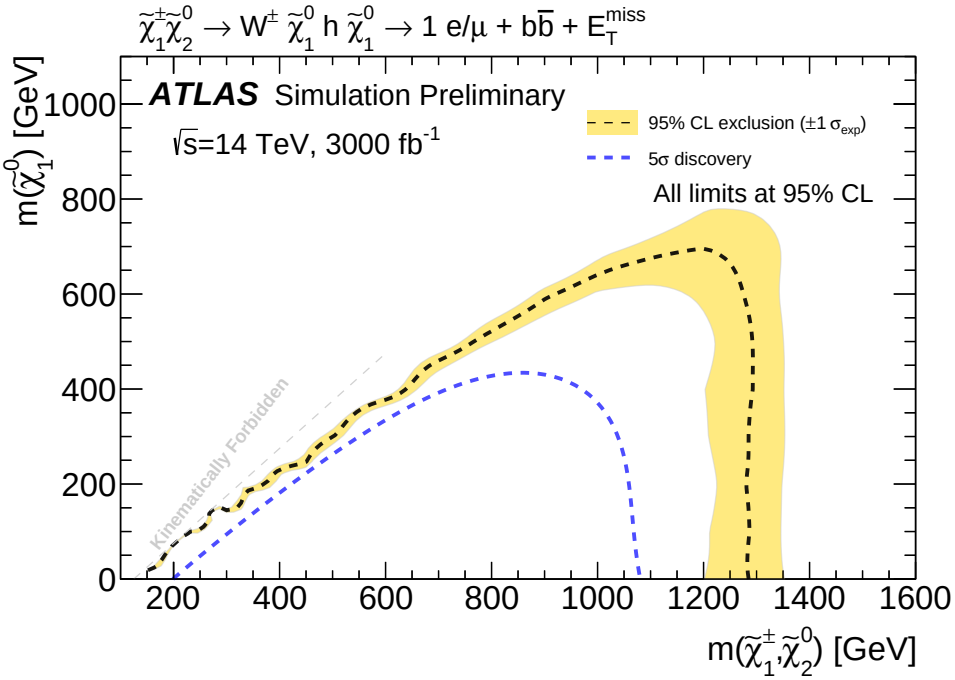

Figure 4.6: 95% CL exclusion limit and 5σ discovery limit for the analysis presented in this chapter.

As shown in Figure 4.6, it is expected that this channel can be excluded upto 1280 GeV, while there is discovery potential upto 1070 GeV. This far exceeds the exclusion limits at the end of Run-2, with results shown in Chapter 1 for both 36.1fb^{-1} and 139fb^{-1}. During this analysis, studies were performed using a both a conventional cut-based analysis and also using a deep neural network to perform binary classification of signal and background. These studies are included in Appendix A.

Appendix A

Sensitivity to $\tilde{\chi}_1^{\pm}\tilde{\chi}_2^0$ pair-production at the HL-LHC

The first part of this appendix is dedicated to documenting the detector simulation parameterisations detailed in Chapter 4.

A.1 Detector simulation parameterisations

Electrons

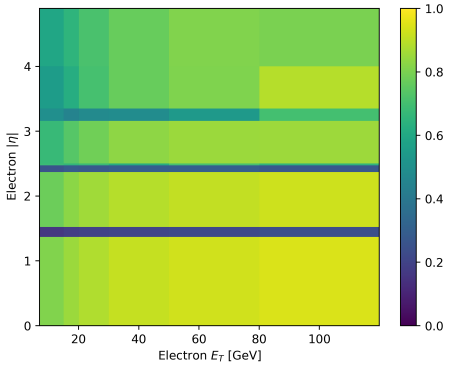

(a) ϵ_{rec} for 'loose' electron working point.

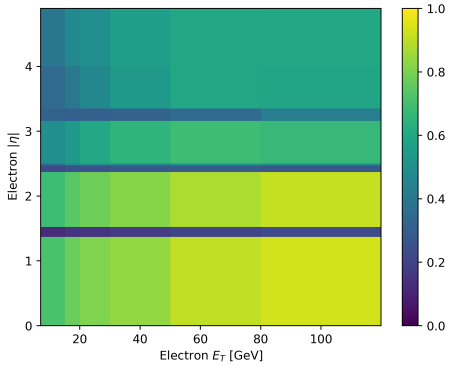

(b) ϵ_{rec} for 'medium' electron working point.

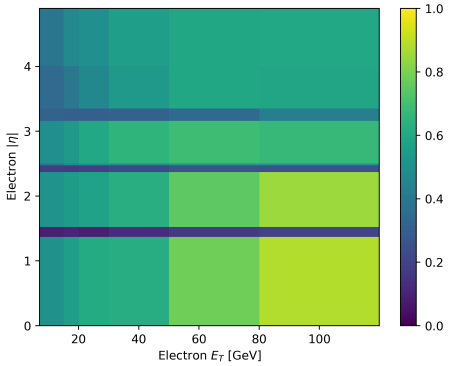

(c) ϵ_{rec} for 'tight' electron working point.

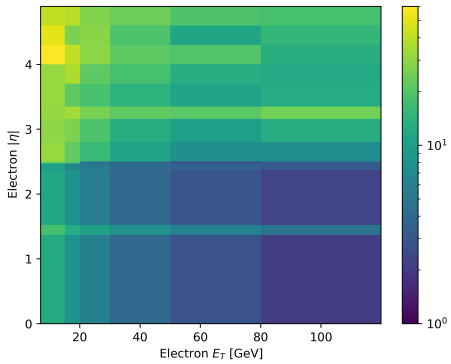

(d) Electron energy resolution (MeV).

Figure A.1: Electron ID efficiencies, energy resolution and charge-flip probability for the prospects study presented in Chapter 4. The

Muons

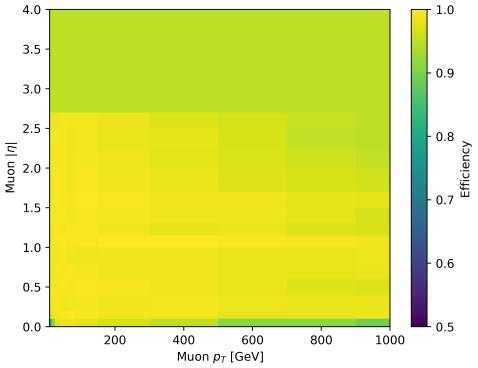

(a) ϵ_{rec} for 'loose' muon working point.

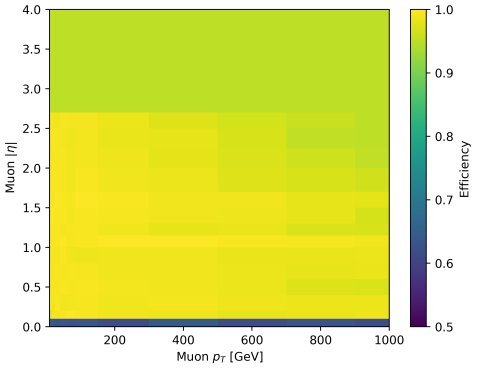

(b) ϵ_{rec} for 'tight' muon working point.

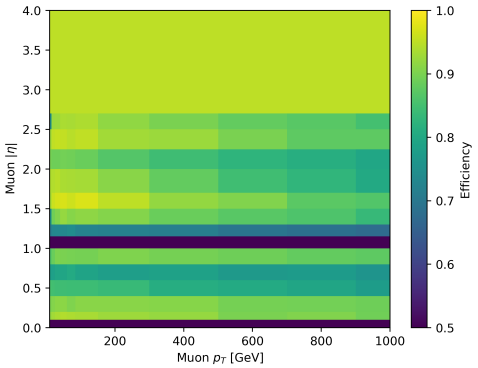

(c) ϵ_{rec} for 'high-p_T' muon working point.

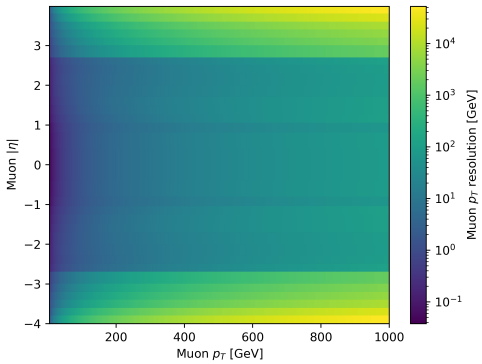

(d) Muon p_T resolution (MeV).

Figure A.2: Muon ID efficiencies and p_T resolution for the prospects study presented in Chapter 4. The

Jets

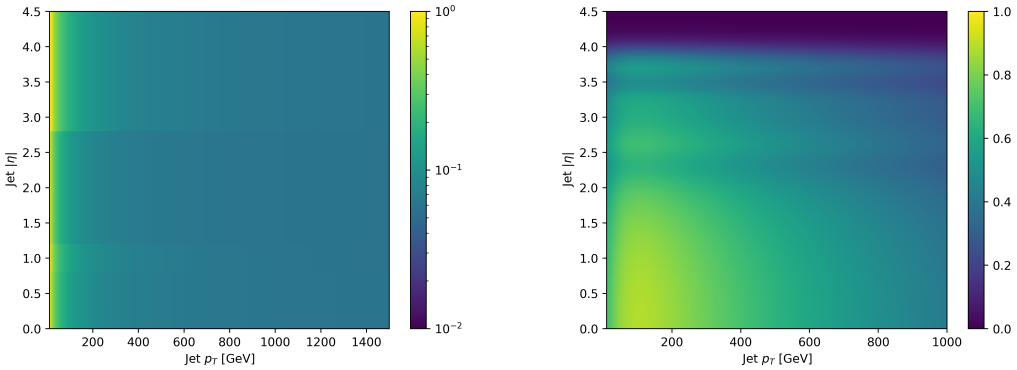

(a) (b)

Figure A.3: Parameterised relative jet energy resolution, shown in Figure A.3a, and parameterised b-tagging efficiency, shown in Figure A.3b, used in the HL-LHC detector simulation.

691 $E_{\mathrm{T}}^{\mathbf{miss}}$

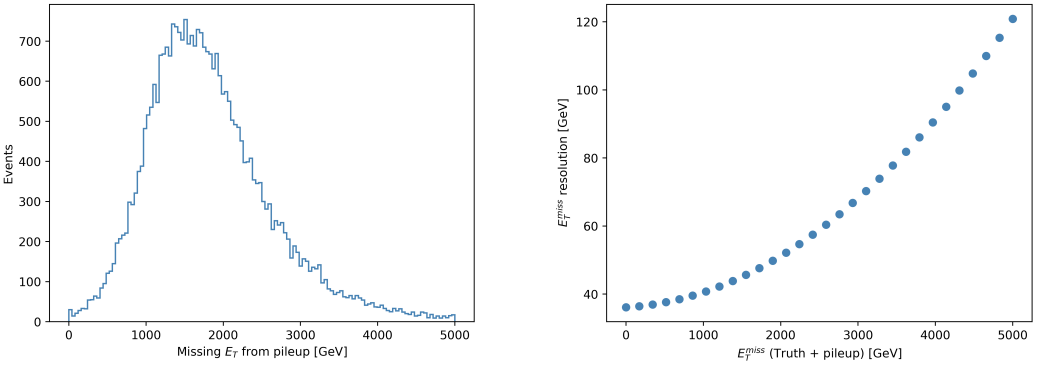

(a) (b)

Figure A.4: Parameterised $E_{\mathrm{T}}^{\mathrm{miss}}$ distribution from pileup, shown in Figure A.4a, and parameterised $E_{\mathrm{T}}^{\mathrm{miss}}$ resolution, shown in Figure A.4b, used in the HL-LHC detector simulation.

A.2 Cut & count studies

A reoptimisation of the signal regions defined in Table 1.2 was performed to compare the potential sensitivity of the conventional analysis to the multivariate analysis described in Chapter 4. During the reoptimisation, the selections on the m_{bb} and m_{CT} variables are unchanged from Table 1.2. A scan over the lower bound of the m_T and E_T^{miss} variables was performed in steps of 10 GeV, with no upper bound. The lack of an upper bound on these variables means the regions are able to overlap, and therefore lose their orthogonality. However, as the final fit result takes the best expected sensitivity for each point, the orthogonality of signal regions is not required. The cuts maximising the binomial significance, Z_n, for the benchmark signal points shown in Table 4.5 are chosen for the three signal regions. These cuts are summarised in Table A.1. The sensitivity to each signal

	SRLM	SRMM	SRHM
m_{bb}	$\in [105, 135]$		
m_{CT}	> 160		
$E_{\mathrm{T}}^{\mathrm{miss}}$	> 320	> 380	> 420
m_{T}	> 180	> 280	> 280

Table A.1: Reoptimised signal region selections for conventional analysis in order to compare sensitivity with the multivariate analysis described in Chapter 4. All cuts are in units of GeV.

point is assessed by calculating the binomial significance, Z_n, for each signal point in all three signal regions, and the combination of the regions takes the best expected significance for each point. The expected sensitivities can be seen in Figure A.5.

A.3 Deep learning studies

In addition to the the reoptimisation of the signal regions, described in the previous section, a study of the expected sensitivity using a DNN as a binary classifier was undertaken. A diagram of the DNN used in this study is shown in Figure A.6, and the model itself is implemented using Keras and Tensorflow. The inputs to the classifier are the same as described in Chapter 4for the BDT analysis, and the same procedure for separating the signal samples into three sets targetting different mass-splitting regimes is also the same. The DNN is trained on a GPU for a maximum of 10000 epochs, or until the accuracy of the classifier, evaluated using test data, has not improved in 2 epochs. To avoid overtraining, a dropout of 20% is used, such that upto 20% of the inputs to each layer can be ignored, at random, in each training epoch. Similarly to the BDT analysis described in Chapter 4, 3 classifiers are trained, one per mass-splitting region. The signal-background discrimination can be seen in Figure A.7.

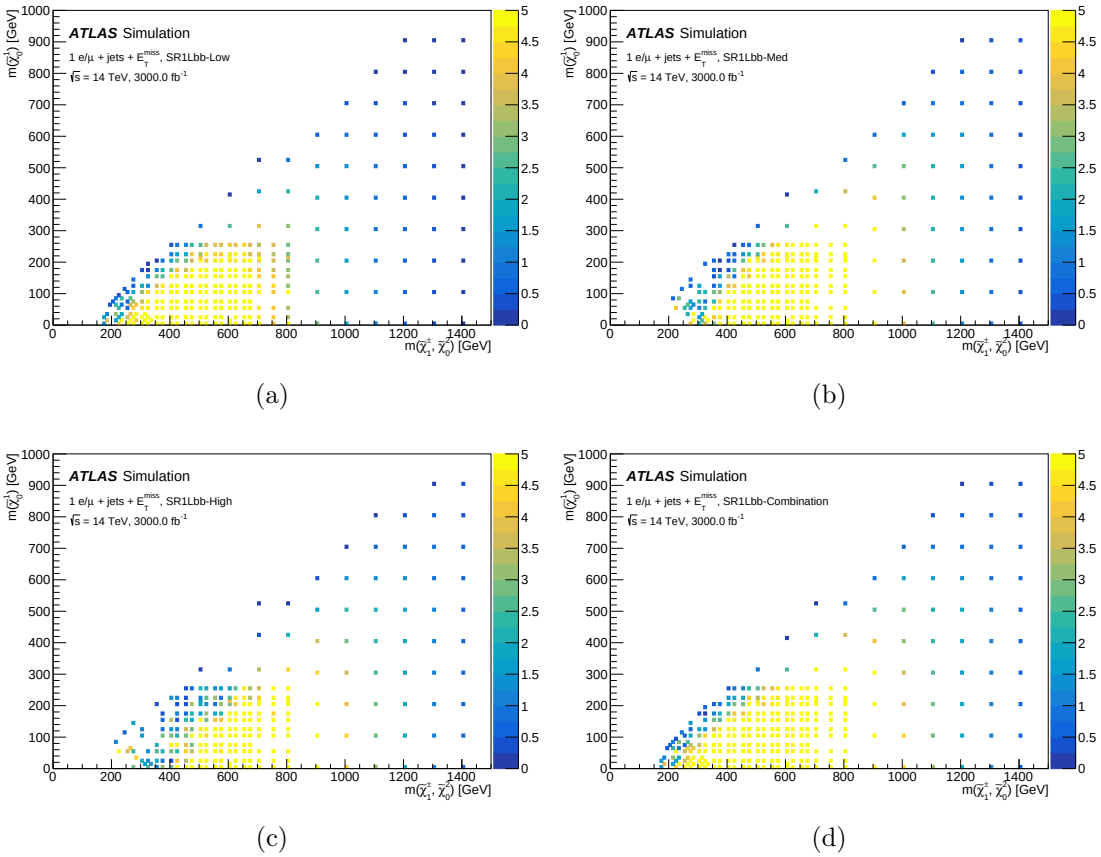

Figure A.5: Plots showing the binomial significance, Z_n, of each signal point in the reoptimised SRLM (A.5a), SRMM (A.5b), SRHM (A.5c), and the best expected combination (A.5d). All plots are produced assuming a total 15% background uncertainty.

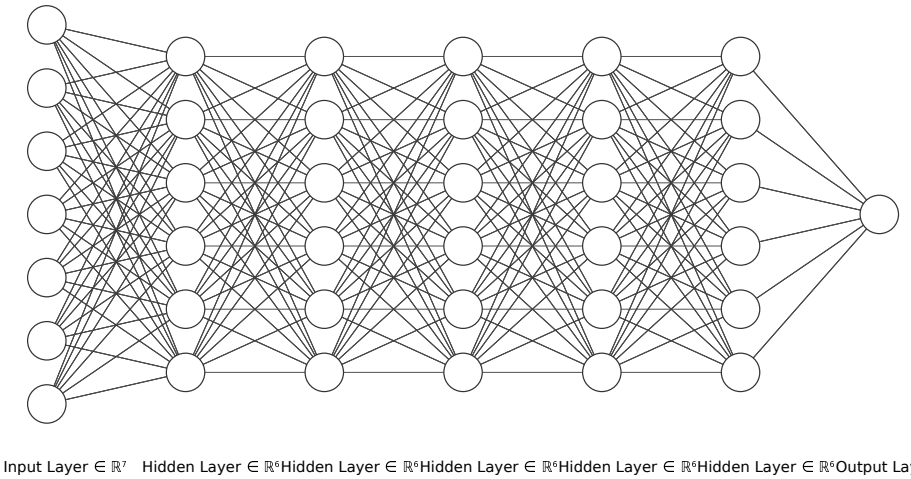

Figure A.6: A diagram showing the structure of the fully-connected Deep Neural Network tested as a binary classifier in the HL-LHC sensitivity study.

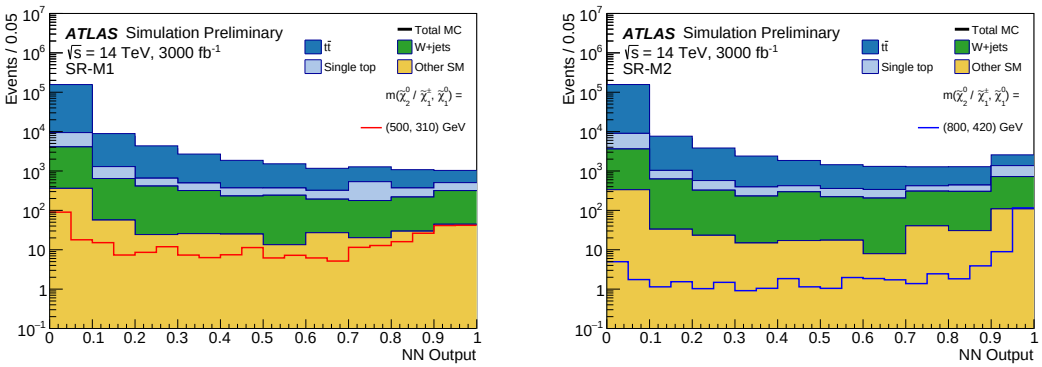

(a)

(b)

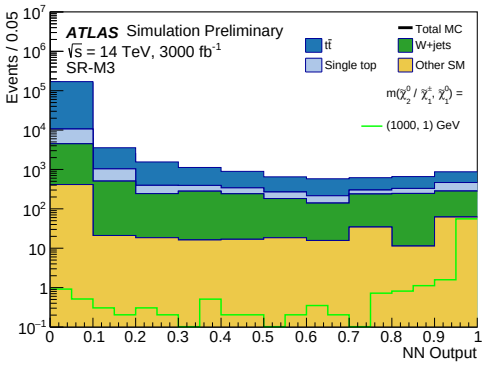

(c)

Figure A.7: Outputs for each of the DNN classifiers trained on the signal ensemble of each region and the dominant $t\bar{t}$ background.

The shape and range of the output of the DNN classifiers is due to the use of the sigmoid/softmax activiation on the output layer of the classifier, while TMVA performs a transformation of the form $y(x) = -\frac{1}{15}\left(\frac{1}{x} - 1\right)$ on the output of the classifier [35]. The DNN classifiers were not used in the final analysis as the sensitivity to the signal using a cut on the output of the DNN classifiers is much lower than for the BDT classifiers. While these studies were not performed due to time and resource constraints, it is expected that with larger MC statistics for the signal samples, fine-tuning of the DNN hyperparameters, and performing multi-class classification instead of binary classification, the DNN could achieve superior classification performance over the BDT classifiers.

A.4 Extending W+jets sample statistics

After applying all selections listed in Table 4.4 and the cuts on the BDT output listed in Table 4.5, the MC statistics in the W+jets sample was extremely low, such that the MC statistical uncertainty was $\sim 100\%$. For the final statistical analysis, a procedure was developed for extending the W+jets sample statistics in order to predict realistic yields and uncertainties. Using the detector simulation method described in Chapter 4, individual events in the nominal W+jets samples were smeared $N = 10$ times, to produce an extended sample with $\leq N$ times the input sample statistics. Due to the significant computing time of running this procedure, only B-filtered slices of the W+jets MC with $W \to e\nu/\mu\nu$ were used as the input for this procedure. A plot comparing the shape of the E_T^{miss} distribution for the nominal B-filtered samples with electrons, muons and taus and extended samples for B-filtered samples with electrons and muons is shown in Figure A.8.

The normalisation of the extended sample is corrected for the multiple smearing method by weighting each event by a factor $\frac{1}{N}$, and corrected for the missing $W \to \ell\nu$ slices by multiplying the expected yield of the extended sample by $N_{MC}^{nominal}/N_{MC}^{extended}$ evaluated at preselection level. The correction factor for the missing MC slices was found to be 1.21.

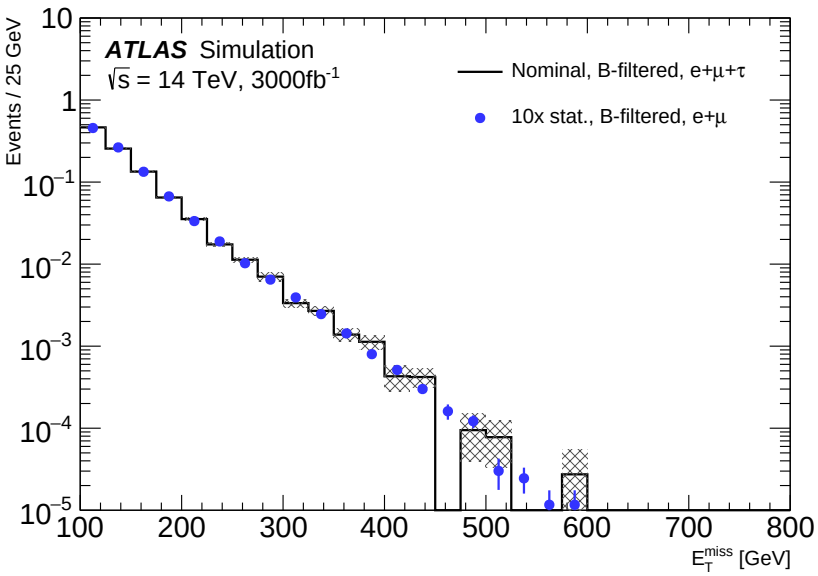

Figure A.8: A comparison of the E_T^{miss} distributions at preselection level for the nominal W+jets sample and the sample with extended MC statistics from the multiple event smearing method described in this section.

Bibliography

[1] Georges Aad et al. Search for direct pair production of a chargino and a neutralino decaying to the 125 GeV Higgs boson in $\sqrt{s} = 8$ TeV pp collisions with the ATLAS detector. *Eur. Phys. J. C*, 75(5):208, 2015.

[2] Johan Alwall, Philip C. Schuster, and Natalia Toro. Simplified models for a first characterization of new physics at the lhc. *Physical Review D*, 79(7), Apr 2009.

[3] Daniele Alves, Nima Arkani-Hamed, Sanjay Arora, Yang Bai, Matthew Baumgart, Joshua Berger, Matthew Buckley, Bart Butler, Spencer Chang, Hsin-Chia Cheng, and et al. Simplified models for lhc new physics searches. *Journal of Physics G: Nuclear and Particle Physics*, 39(10):105005, Sep 2012.

[4] ATLAS Collaboration. Search for chargino-neutralino production using recursive jigsaw reconstruction in final states with two or three charged leptons in proton-proton collisions at $\sqrt{s} = 13$ TeV with the ATLAS detector. *Phys. Rev. D*, 98(9):092012, 2018.

[5] ATLAS Collaboration. Search for chargino-neutralino production with mass splittings near the electroweak scale in three-lepton final states in $\sqrt{s} = 13$ tev pp collisions with the atlas detector. *Physical Review D*, 101, 04 2020.

[6] Georges Aad et al. Search for direct production of electroweakinos in final states with one lepton, missing transverse momentum and a Higgs boson decaying into two b-jets in pp collisions at $\sqrt{s} = 13$ TeV with the ATLAS detector. *Eur. Phys. J. C*, 80(8):691, 2020.

[7] Search for dark matter associated production with a single top quark in $\sqrt{s} = 13$ TeV (pp) collisions with the ATLAS detector. Technical Report ATLAS-CONF-2020-034, CERN, Geneva, Aug 2020.

[8] Jalal Abdallah, Adi Ashkenazi, Antonio Boveia, Giorgio Busoni, Andrea De Simone, Caterina Doglioni, Aielet Efrati, Erez Etzion, Johanna Gramling, Thomas Jacques, Tongyan Lin, Enrico Morgante, Michele Papucci, Bjoern Penning, Antonio Walter Riotto, Thomas Rizzo, David Salek, Steven Schramm, Oren Slone, Yotam Soreq,

Alessandro Vichi, Tomer Volansky, Itay Yavin, Ning Zhou, and Kathryn Zurek. Simplified models for dark matter and missing energy searches at the lhc, 2014.

[9] Jalal Abdallah, Henrique Araujo, Alexandre Arbey, Adi Ashkenazi, Alexander Belyaev, Joshua Berger, Celine Boehm, Antonio Boveia, Amelia Brennan, Jim Brooke, and et al. Simplified models for dark matter searches at the lhc. *Physics of the Dark Universe*, 9-10:8–23, Sep 2015.

[10] Daniel Abercrombie, Nural Akchurin, Ece Akilli, Juan Alcaraz Maestre, Brandon Allen, Barbara Alvarez Gonzalez, Jeremy Andrea, Alexandre Arbey, Georges Azuelos, Patrizia Azzi, and et al. Dark matter benchmark models for early lhc run-2 searches: Report of the atlas/cms dark matter forum. *Physics of the Dark Universe*, 27:100371, Jan 2020.

[11] Priscilla Pani and Giacomo Polesello. Dark matter production in association with a single top-quark at the lhc in a two-higgs-doublet model with a pseudoscalar mediator. *Physics of the Dark Universe*, 21:8–15, Sep 2018.

[12] Felix Kahlhoefer, Kai Schmidt-Hoberg, Thomas Schwetz, and Stefan Vogl. Implications of unitarity and gauge invariance for simplified dark matter models. *Journal of High Energy Physics*, 2016(2), Feb 2016.

[13] `url: http://feynrules.irmp.ucl.ac.be/wiki/DMsimp`.

[14] Tomohiro Abe, Yoav Afik, Andreas Albert, Christopher R. Anelli, Liron Barak, Martin Bauer, J. Katharina Behr, Nicole F. Bell, Antonio Boveia, Oleg Brandt, Giorgio Busoni, Linda M. Carpenter, Yu-Heng Chen, Caterina Doglioni, Alison Elliot, Motoko Fujiwara, Marie-Helene Genest, Raffaele Gerosa, Stefania Gori, Johanna Gramling, Alexander Grohsjean, Giuliano Gustavino, Kristian Hahn, Ulrich Haisch, Lars Henkelmann, Junji Hisano, Anders Huitfeldt, Valerio Ippolito, Felix Kahlhoefer, Greg Landsberg, Steven Lowette, Benedikt Maier, Fabio Maltoni, Margarete Muehlleitner, Jose M. No, Priscilla Pani, Giacomo Polesello, Darren D. Price, Tania Robens, Giulia Rovelli, Yoram Rozen, Isaac W. Sanderson, Rui Santos, Stanislava Sevova, David Sperka, Kevin Sung, Tim M. P. Tait, Koji Terashi, Francesca C. Ungaro, Eleni Vryonidou, Shin-Shan Yu, Sau Lan Wu, and Chen Zhou. Lhc dark matter working group: Next-generation spin-0 dark matter models, 2018.

[15] M. Aaboud, G. Aad, B. Abbott, D. C. Abbott, O. Abdinov, D. K. Abhayasinghe, S. H. Abidi, O. S. AbouZeid, N. L. Abraham, and et al. Constraints on mediator-based dark matter and scalar dark energy models using $\sqrt{s} = 13$ tev pp collision data collected by the atlas detector. *Journal of High Energy Physics*, 2019(5), May 2019.

[16] T Kawamoto, S Vlachos, L Pontecorvo, J Dubbert, G Mikenberg, P Iengo, C Dallapiccola, C Amelung, L Levinson, R Richter, and D Lellouch. New Small Wheel

Technical Design Report. Technical Report CERN-LHCC-2013-006. ATLAS-TDR-020, Jun 2013. ATLAS New Small Wheel Technical Design Report.

[17] The ATLAS Collaboration. Technical Design Report for the Phase-I Upgrade of the ATLAS TDAQ System. Technical Report CERN-LHCC-2013-018. ATLAS-TDR-023, Sep 2013. Final version presented to December 2013 LHCC.

[18] Technical Design Report for the ATLAS Inner Tracker Pixel Detector. Technical Report CERN-LHCC-2017-021. ATLAS-TDR-030, CERN, Geneva, Sep 2017.

[19] Technical Design Report for the ATLAS Inner Tracker Strip Detector. Technical Report CERN-LHCC-2017-005. ATLAS-TDR-025, CERN, Geneva, Apr 2017.

[20] Expected Tracking Performance of the ATLAS Inner Tracker at the HL-LHC. Technical Report ATL-PHYS-PUB-2019-014, CERN, Geneva, Mar 2019.

[21] R. Diener, J. Dreyling-Eschweiler, H. Ehrlichmann, I.M. Gregor, U. Kötz, U. Krämer, N. Meyners, N. Potylitsina-Kube, A. Schütz, P. Schütze, and et al. The desy ii test beam facility. *Nuclear Instruments and Methods in Physics Research Section A: Accelerators, Spectrometers, Detectors and Associated Equipment*, 922:265–286, Apr 2019.

[22] Hendrik Jansen, Simon Spannagel, Jörg Behr, Antonio Bulgheroni, Gilles Claus, Emlyn Corrin, David Cussans, Jan Dreyling-Eschweiler, Doris Eckstein, Thomas Eichhorn, and et al. Performance of the eudet-type beam telescopes. *EPJ Techniques and Instrumentation*, 3(1), Oct 2016.

[23] M. Garcia-Sciveres, D. Arutinov, M. Barbero, R. Beccherle, S. Dube, D. Elledge, J. Fleury, D. Fougeron, F. Gensolen, D. Gnani, V. Gromov, T. Hemperek, M. Karagounis, R. Kluit, A. Kruth, A. Mekkaoui, M. Menouni, and J.-D. Schipper. The fe-i4 pixel readout integrated circuit. *Nuclear Instruments and Methods in Physics Research Section A: Accelerators, Spectrometers, Detectors and Associated Equipment*, 636(1, Supplement):S155 – S159, 2011. 7th International ""Hiroshima"" Symposium on the Development and Application of Semiconductor Tracking Detectors.

[24] Maurice Garcia-Sciveres. The RD53A Integrated Circuit. Technical Report CERN-RD53-PUB-17-001, CERN, Geneva, Oct 2017.

[25] Study of the double Higgs production channel $H(\to b\bar{b})H(\to \gamma\gamma)$ with the ATLAS experiment at the HL-LHC. Technical Report ATL-PHYS-PUB-2017-001, CERN, Geneva, Jan 2017.

[26] Jung Chang, Kingman Cheung, Jae Sik Lee, and Jubin Park. Probing the trilinear Higgs boson self-coupling at the high-luminosity LHC via multivariate analysis. *Phys. Rev. D*, 101(1):016004, 2020.

[27] M. Cepeda et al. *Report from Working Group 2: Higgs Physics at the HL-LHC and HE-LHC*, volume 7, pages 221–584. 12 2019.

[28] Xabier Cid Vidal et al. *Report from Working Group 3: Beyond the Standard Model physics at the HL-LHC and HE-LHC*, volume 7, pages 585–865. 12 2019.

[29] J. Alwall, R. Frederix, S. Frixione, V. Hirschi, F. Maltoni, O. Mattelaer, H.-S. Shao, T. Stelzer, P. Torrielli, and M. Zaro. The automated computation of tree-level and next-to-leading order differential cross sections, and their matching to parton shower simulations. *Journal of High Energy Physics*, 2014(7), Jul 2014.

[30] Torbjörn Sjöstrand, Stefan Ask, Jesper R. Christiansen, Richard Corke, Nishita Desai, Philip Ilten, Stephen Mrenna, Stefan Prestel, Christine O. Rasmussen, and Peter Z. Skands. An introduction to pythia 8.2. *Computer Physics Communications*, 191:159–177, Jun 2015.

[31] ATLAS Run 1 Pythia8 tunes. Technical Report ATL-PHYS-PUB-2014-021, CERN, Geneva, Nov 2014.

[32] Stefano Carrazza, Stefano Forte, and Juan Rojo. Parton distributions and event generators, 2013.

[33] Leif Lönnblad and Stefan Prestel. Merging multi-leg nlo matrix elements with parton showers. *Journal of High Energy Physics*, 2013(3), Mar 2013.

[34] Christoph Borschensky, Michael Krämer, Anna Kulesza, Michelangelo Mangano, Sanjay Padhi, Tilman Plehn, and Xavier Portell. Squark and gluino production cross sections in pp collisions at $\sqrt{s} = 13, 14, 33$ and 100 tev. *The European Physical Journal C*, 74(12), Dec 2014.

[35] A. Hoecker, P. Speckmayer, J. Stelzer, J. Therhaag, E. von Toerne, H. Voss, M. Backes, T. Carli, O. Cohen, A. Christov, D. Dannheim, K. Danielowski, S. Henrot-Versille, M. Jachowski, K. Kraszewski, A. Krasznahorkay Jr., M. Kruk, Y. Mahalalel, R. Ospanov, X. Prudent, A. Robert, D. Schouten, F. Tegenfeldt, A. Voigt, K. Voss, M. Wolter, and A. Zemla. Tmva - toolkit for multivariate data analysis, 2007.